



Sandra Priska Hager, BSc.

**A crack phase-field
approach
to model
aortic dissections**

MASTER'S THESIS

to achieve the university degree of

Master of Science

Master's degree programme: Biomedical Engineering

submitted to

Graz University of Technology

Supervisor

Professor Gerhard A. Holzapfel

Institute of Biomechanics

Co. Supervisor
Osman Gültekin, MSc.

Graz, November 2018

AFFIDAVIT

I declare that I have authored this thesis independently, that I have not used other than the declared sources/resources, and that I have explicitly indicated all material which has been quoted either literally or by content from the sources used. The text document uploaded to TUGRAZonline is identical to the present master's thesis dissertation.

Date

Signature

Contents

Abstract	IX
Zusammenfassung	XI
Acknowledgment	XIII
1. Introduction	1
1.1. Arterial histology	1
1.2. Aortic dissection	2
1.2.1. General aspects of the disease	2
1.2.2. Experiments	6
1.2.3. Numerical studies	7
1.2.4. Fracture mechanics	7
2. Methods	9
2.1. Multi-field framework for fracture	9
2.1.1. Kinematics of mechanical problem	9
2.1.2. Geometrical approach for anisotropic rupture	11
2.2. Strong form of the multi-field problem	13
3. Results	18
3.1. Parameter identification	18
3.2. Parameter validation of the healthy medial sub-layer	21
3.3. Sensitivity of a crack path related to the anisotropy in the material	25
3.4. Application to aortic dissection	30
3.4.1. Geometry and material	30
3.4.2. Mesh and fiber direction	33
3.4.3. Boundary and loading conditions	34
3.4.4. Simulation and numerical results	36
4. Conclusion	39
Bibliography	45

Appendices	47
A. Modeling of soft biological tissue in the Lagrangian configuration	49
A.1. Incompressible material	49
A.1.1. Helmholtz free energy $\Psi(J, I_1, I_4, I_6)$	49
A.1.2. Stress tensor \mathbf{S}	50
A.1.3. Elasticity tensor \mathbb{C}	51
B. Implementation in a finite element code	52
B.1. Temporal discretization	52
B.2. Spatial discretization	52
B.2.1. Spatial discretization for the mechanical problem	53
B.2.2. Spatial discretization for the phase-field problem	53

Abstract

An aortic dissection is detected in 2 to 3.5 out of 100,000 people every year. This type of disease in the aortic wall can appear in an acute or a chronic form and can proceed with a fatal outcome if not treated. An aortic dissection is generally caused by a minimal defect in the intima, which can occur due to an accident or other traumatic events. During a pumping cycle, the aorta undergoes various deformations, such as extension, torsion and inflation. This deformation allows the initially minimal defect to spread inside the aortic wall and generate a second pathway for the blood inside the wall of the artery. The aim of this study is to numerically simulate the crack formation between two medial sub-layers and to determine important parameters for crack formation in a physical environment. The thermodynamic approach for the crack phase-field of fracture developed by Miehe et al. (2010) for an isotropic material is used as a basis for crack propagation modeling.

Since the aorta is a highly anisotropic material it is necessary to expand the model presented by Miehe et al. (2010), which was done by Gültekin et al. (2017). To validate the model of Gültekin et al. (2017) for anisotropic materials, the results were compared with the geometrically anisotropic model of Teichtmeister et al. (2017). In the same study, the sensitivity of the model proposed by Gültekin et al. (2017) in terms of anisotropy parameters was also analyzed. In the next step, the model from Gültekin et al. (2017) was applied to a cylinder, with the dimensions of an aorta (Mao et al., 2008). This cylinder consists of six sub-layers; four layers show the material parameters of a medial layer including a diseased one and the other two layers correspond to the adventita layer. For the simulation of an aortic dissection, an incision in the mesh of the cylinder with different lengths and widths up to the diseased media layer was implemented and then a pumping cycle was simulated in the physiological and supra-physiological range. It was found that with the same deformation, the dissection spreads further in the case of a larger initial defect in the intima. In addition, it was also found that the crack spread helical in the aorta, indicating that the crack arranges itself along the fiber direction in the material.

Zusammenfassung

Jährlich wird in 2 bis 3,5 von 100.000 Menschen eine Aorten Dissektion festgestellt. Diese Erkrankung in der Aortenwand kann sich in ihrer akuten oder chronischen Form äußern und kann bei nicht Behandlung tödlich enden. Eine Aortendissektion wird in der Regel durch einen minimalen Defekt in der Intima, welche durch einen Unfall oder durch ein anderes traumatisches Ereignis auftreten kann, verursacht. Während eines Pumpzyklus wiederfährt die Aorta unterschiedliche Verformungen, wie zum Beispiel Streckung, Torsion und Inflation. Diese Deformationen ermöglichen es, dass sich der anfangs minimale Defekt innerhalb der Aortenwand ausbreiten kann, dies erzeugt einen zweiten Weg für das Blut innerhalb der Arterienwand. Das Ziel dieser Studie ist es die Rissbildung zwischen zwei medialen Unterschichten auf numerische Weise zu simulieren und daraus wichtige Parameter für die Rissbildung in der physiologischer Umgebung zu bestimmen. Als Basis für die Modellierung der Rissausbreitung wird der thermodynamische Ansatz des Crack Phase-Field für Risse, welcher von Miehe et al. (2010) für ein isotropes Material entwickelt wurde verwendet. Da die Aorta ein hoch anisotropes Material darstellt, ist es nötig das von Miehe et al. (2010) vorgestellte Modell zu erweitern, was von Gültekin et al. (2017) durchgeführt wurde. Um das Modell von Gültekin et al. (2017) für anisotrope Materialien zu validieren, wurden die Resultate mit dem geometrisch anisotropen Modell von Teichtmeister et al. (2017) verglichen. In der selben Studie, konnte auch die Sensitivität des Modells (Gültekin et al., 2017) im Bezug auf die Anisotropieparameter analysiert werden. Im darauffolgenden Schritt wurde das Modell (Gültekin et al., 2017) auf einen Zylinder angewandt, mit den Dimensionen einer menschlichen Aorta (Mao et al., 2008). Dieser Zylinder setzt sich aus insgesamt sechs Unterschichten zusammen; vier Schichten weisen die Materialparameter einer medialen Schicht auf, darunter befindet sich eine erkrankte Schicht und die weiteren zwei Schichten wurden mit Materialparametern einer adventitiären Schicht simuliert. Für die Simulation einer Aortendissektion wurde ein Einschnitt in der Mesh des Zylinders, mit unterschiedlicher Länge und Breite bis zur kranken Mediaschicht, implementiert und dann ein einzelner Pumpzyklus im physiologischen und ein weiterer im supra-physiologischen Bereich simuliert. Bei den Resultaten dieser Simulation konnte festgestellt werden, dass sich bei gleicher Deformation, die Dissektion weiter ausbreitet im Falle eines größeren Anfangsdefekts in der Intima. Zusätzlich konnte man feststellen, dass sich der Riss helikal in der Aorta ausbreitet, was darauf hinweist, dass sich der Verlauf eines Risses an die Faserrichtung im Material anpasst.

Acknowledgment

At this point I would like to thank Professor Gerhard A. Holzapfel from the Institute of Biomechanics at Graz University of Technology for the opportunity to deal with the topic of modeling in biomechanics and the enabled me to write this thesis through his supervision. Especially, I would like to thank Osman Gültekin for his active support and supervision during the time I have done my master thesis. Also I want to thank him for the opportunity to work with him on a paper and that I had the chance to learn a lot from him. I am grateful that I had the opportunity to continue my education in an area that also reflects my interests.

I would also like to thank all my colleagues at the Institute of Biomechanics who have assisted me in word and deed over the past months.

Above all, I would like to thank my mother, Monika, my brother, Karl, and my stepfather, Klaus, who always support me in all life situations and always give me back my faith in myself. Furthermore, I would like to thank my late father, Karl, that he always believed in me and showed me to strive for great things.

Last but not least I would like to thank all my friends, those I already know for decades and also those who accompanied me through my studies and motivated me again and again.

Sandra Priska Hager

1. Introduction

1.1. Arterial histology

Aortic dissection describes the process of delamination, or better known as separation of the aortic wall. To understand this process, it is important to understand the internal architecture of the aortic wall. Elastic arteries, in general, which also includes the aorta, consists of three different main layers. These layers are arranged around the inner volume of an artery called lumen. In the aorta, the lumen acts as the main pathway for the blood transport through the body. The wall of an artery consists, in general, of three main layers, each of these differs from the other by certain properties, Fig. 1.1 shows a general overview of the internal structure from a healthy artery.

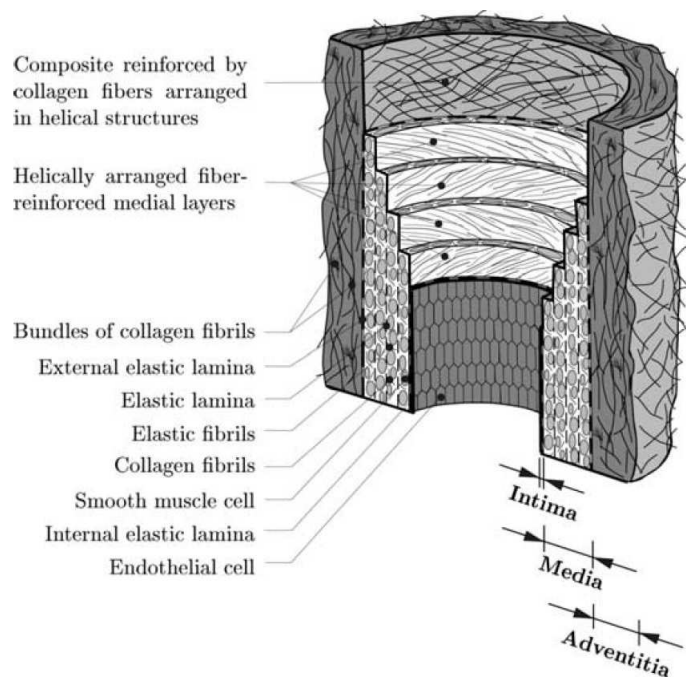


Figure 1.1.: Structure of a healthy human artery, composed of the different main layers intima, media and adventitia, and several collagenous sub-layers separated by elastic lamina sheets. Adapted from Holzapfel et al. (2000).

The innermost layer, related to the lumen, consists of a mono-layer of endothelial cells and is additionally supported by a fairly loose connective tissue, referred to as tunica intima. Since this layer is in direct contact with the blood stream, which transports essential

nutrients for the body, it is an important interface for the metabolic processes inside the body (Mussa et al., 2016). On the exterior side the intima is limited by the interna elastic lamina, these elastic lamina enables the movement of the intima in relation to the other main layers of the artery during a cardiac cycle [Holzapfel et al. (2000), Gasser et al. (2006), Ross and Pawlina (2011)].

The mid-layer, the thickest of the three main layers, is called tunica media. This muscular layer supports the aortic wall against the blood pressure from the inside of the artery, with its contained smooth muscle cell layers and the collagenous fiber network. In an adult person, the media consists of 40 to 70 sub-layers of fenestrated, lamellar elastin sheets, which separates the smooth muscle cell layers. The number of this sheets varies between age and blood pressure of a person, e.g., in a person with hypertension the number and thickness of the layers are increased. These fibers and sheets are further embedded in a ground substance of proteoglycans. The collagen fibers are assumed to be helically oriented in a single sub-layer to limit the extension of the artery during the systolic phase of the cardiac cycle and contribute to the mechanical properties of an artery. The contraction phase of a cardiac cycle is defined as systole, in which the left ventricle releases and pumps the blood in the aorta. Schriefl et al. (2012) observed in their study that the media comprises two collagen fiber families which are organized different in the separate layers. This leads to the assumption that each layer contains only of one preferred fiber direction. In addition, the smooth muscle cells are aligned in a circumferential and coherent manner in the media to distribute the blood in the body through the controlled contraction of the artery. At the interface between the media and the last main layer, called adventitia, lies the *external elastic lamina* [Holzapfel et al. (2000), Gasser et al. (2006), Ross and Pawlina (2011), Mussa et al. (2016)].

The tunica adventitia characterizes the outermost layer of the aorta that keeps the aorta at its place in the body. This layer is relatively thin, less than the half of the media thickness. It consists of collagen and elastic fibers, which form a fairly loose network, fibroblasts and macrophages. The collagen fibers are arranged in a helical structure, these fibers are in general stiffer than those in the media. Due to the smooth transition of the actual adventitial layer to the connective tissue, an absolute distinction cannot easily be made [Holzapfel et al. (2000), Gasser et al. (2006), Ross and Pawlina (2011)].

1.2. Aortic dissection

1.2.1. General aspects of the disease

Based on the knowledge of the inner structure of the aorta, the process of aortic dissection can now be studied more closely. An aortic dissection describes the loose of the structural integrity in the artery wall, which means a change of the inner structure of the artery seen in Fig. 1.1. As a result, the mechanical reaction to a load in the diseased aortic wall decreases. It is assumed that one of the main causes of an aortic dissection is hypertension, which refers to a high blood pressure inside the artery. This condition is diagnosed

in around 70 percent (Sommer et al., 2016) of the aortic dissection cases. A further common reason for aortic dissection is a disease of the connective tissue in the aortic wall, e.g., Marfan–syndrome (Mussa et al., 2016). An aortic dissection could be also caused by a previous injury of the aorta, e.g., after a car accident or a consequence of an incision caused by a cardiac catheterization (Dunning et al., 2000). IRAD (IRAD, 1996), the International Registry of acute aortic dissection, proclaims that men, between the age of 48 and 67, are three times more susceptible to aortic dissection than woman. Related to western countries the rate of aortic dissection is 2 to 3.5 out of 100,000 people (Hiratzka and Bakris, 2010).

In the case of an occurrence of an aortic dissection the initial phase is defined by a formation of a tear in the intima. The cause of this kind of defect of the structural integrity of the vascular wall in the physiological range is still unclear. An aortic dissection may also appear in the absence of this tear where the dissection starts to propagate from an intermural haemorrhage or a haematoma formation in the media. One of the assumptions about the formation of an initial tear is that it forms due to high hemodynamic forces at certain locations of the aorta (Numata et al., 2016). Cherry and Dake (2009) observed previously mentioned high hemodynamic forces, for instance, at the root of the aortic arch and right after the origin of the left subclavian artery. Especially, the left subclavian artery, which supplies the left arm with oxygenated blood exhibits large turbulences of the blood stream in the aorta. Through the turbulences additional large stress are generated in the tissue and facilitate the tearing of the thin endothelial liner of the intima [Mussa et al. (2016), Numata et al. (2016), Cherry and Dake (2009)].

Starting from an initial tear, the high stress in the tissue can lead to a fracture initiation at locations with high hemodynamic forces, which was observed by Numata et al. (2016). These cracks can then propagate either in the radial direction towards the media, observed by Mikich (2003), or helically along the longitudinal direction between two sub–layers of media and also propagate towards the adventitia. Since cracks cannot easily propagate through multiple fibrils, which would be the case for the crack propagation in the radial direction, it is more likely that the crack propagates along two sub–layers, as mentioned by Schriebl et al. (2012). Based on this knowledge, the focus of this study is the modeling of an aortic dissection along sub–layers of the media.

From the lumen of the aorta a significant amount of the bloodstream can enter the dissected part between these layers of the artery wall through the initial tear. This creates a second channel for the bloodstream the so–called false lumen, see Fig. 1.2. Blood enters the wall through an initial tear and continues to shear away the connection between the two neighboring medial sub–layers. With each systole of the heart, blood jets through this tear and cause even more tearing. From this point on, the dissection can continue its propagation along the aorta or can create a so–called exit tear, also referred to as secondary tears so that the blood can flow back into the aorta. In the absence of an exit tear, more and more blood enters the false lumen. Over time the false lumen takes a significant amount of space in the aorta, which decreases the blood volume through the true lumen. Consequently, the blood supply in the whole body is disturbed and the tissue is not supplied with sufficient nutrients, which further leads to the necrosis of the cells. An other outcome of this situation

is that the remaining artery wall between the false lumen and the adventitia will undergo a dilatation and weakening over time, which can lead to other severe pathologies in the false lumen, for example rupturing of the remaining aortic wall [Mussa et al. (2016), Cherry and Dake (2009)].

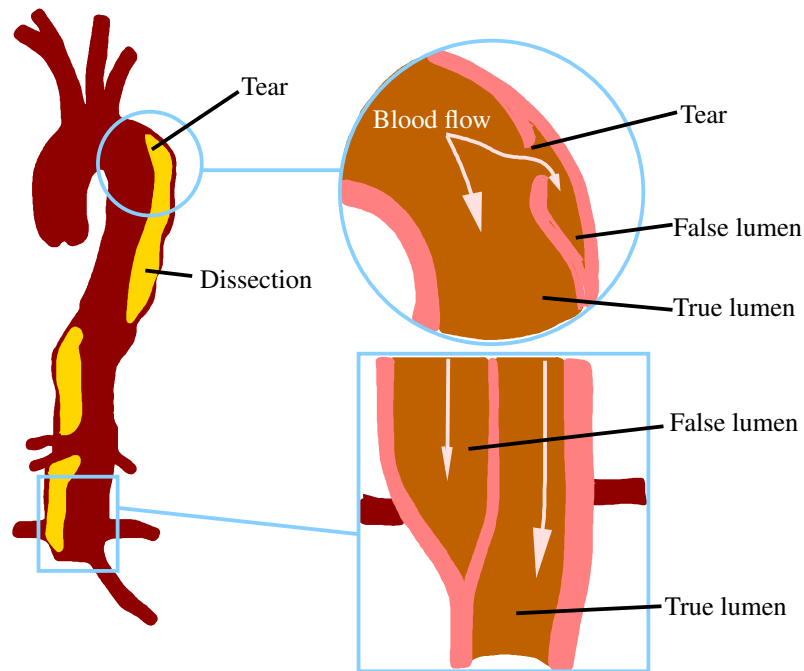


Figure 1.2.: Aortic dissection in the descending part of the aorta, with an initial tear which allows that the blood enters the aortic wall. With every cardiac cycle the left ventricle jets blood into the dissected part of the aorta and separates the wall more and more. This separation of the wall layers leads to the creation of a second blood channel, called false lumen beside the true lumen. With the ungoing dissection the heart jets even more blood in the false lumen. Adapted from: <https://www.cardiachealth.org/aortic-dissection-type-b-complications/> (20.01.2018).

Classification of an aortic dissection

Despite the characterization of an aortic dissection based on the duration it commences until the time it is diagnosed, referred to as acute or chronic. There are two main classification systems to distinguish an aortic dissection, as illustrated in Fig. 1.3. The Stanford classification defines whether the lesion affects either the ascending segment of the aorta, the part until the origin of the left subclavian artery (Type A) or the descending part of aorta (Type B), which is localized after the origin of the left subclavian artery. The DeBakey system, on the other hand, classifies 3 different types of aortic dissection; Type I of the DeBakey classification describes the pathology affecting the ascending and descending

part of the aorta, whereas Type II describes only the ascending segment of the aorta affected by the dissection and Type III classifies an aortic dissection affecting the descending segment of the aorta [Hiratzka and Bakris (2010)].

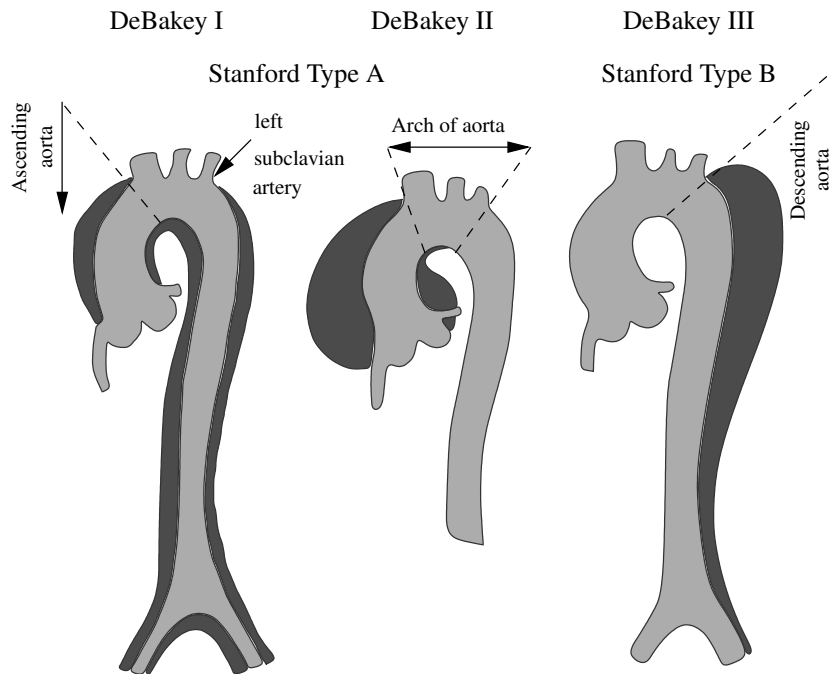


Figure 1.3.: Classification of the aortic dissection types by the affected region of the aorta. Stanford Type A describes if the ascending aorta is affected by the delamination of the aortic wall, or if the dissection starts in the descending aorta (Stanford Type B). In comparison to Stanford Type A, which only describes if the ascending part is affected or not, the DeBakey I and DeBakey II additionally differentiate if the entire aorta is affected or only the ascending part of the aorta. Furthermore, DeBakey III defines a dissection just in the descending area of the aorta. Adapted from: Tsamis et al. (2013).

Treatment of an aortic dissection

The type of classification of an aortic dissection, mentioned in Chapter 1.2.1, has a major implication on the treatment of it. Type A, is the most common type of aortic dissection. Due to its location there are extremely large shear stresses caused by the jet of blood from the left ventricle of the heart during the systolic phase. The treatment plan always considers surgery. The aim of this procedure is in replacing the affected part of the aorta with an endograft. This endograft is exactly placed and stitched under the remaining part of the false lumen, to seal it and stop the blood to enter the false lumen. For a better fixation of the endograft the aorta is surrounded with a teflon felt on the outside. To make this endograft also leak proof, tissue engineered collagen fibers are built in the device. Type B,

on the other hand, is treated with medication to lower the blood pressure by decreasing the heart rate and the contractility. In the case of complications with the conservative method a minimal invasive surgery to treat this type of aortic dissection is possible. Previous mentioned method describes an endovascular stent grafting, where a stent is directly implanted in the dissected part of the descending aorta to treat the dissected part of the aorta [Pepper (2016)].

1.2.2. Experiments

Initial tear

Carson and Roach (1990) performed experiments on the healthy thoracic pig aorta with the aim to investigate the mechanical properties, for which a bleb (a bubble inside the aortic wall) was prescribed in the tunica media. They observed that the generation of this kind of bleb in healthy arteries needed very high non-physiological hydraulic pressure. The initiation of aortic dissection could also occur in the physiological range of the blood pressure in the artery and further facilitate a propagation of the dissection inside the healthy tissue of the aorta. For this observation they took samples which already showed a peak in the shear force under physiological conditions. The tissue of the right lateral wall, located in the ascending part of the thoracic aorta or the descending thoracic aorta directly after the *ligamentum arteriosum*, are known as locations for high stresses in the tissue and further for developing an aortic dissection (Kasper et al., 2015).

Dissection

Van Baardwijk and Roach (1987) intended to observe that the crack propagation after an initial tear was formed. Their experiments showed that the development of an dissection is dependent on the depth of the initial tear in the radial direction and also related to the pressure gradient over the arterial wall. Dissections which were located closer to the intimal surface developed faster than those which were closer to the adventitia. They assumed that this behavior could also depend on the anisotropic behavior of the media with different radial depth in the aorta. Due to that an aortic dissection describes actually a delamination of the aortic wall, Sommer et al. (2008) performed a steady state investigation by the use of a peeling test. This allowed an investigation of a slow and controlled propagation of a dissection inside the artery. During the experiment they have shown that the damage spreads over approximately 6 to 7 elastic laminae. Later, Sommer et al. (2016) measured the ‘in-plane’ shear stress in the tissue and realized that this shear mode is the most common reason for arterial wall failures other than the ‘out-plane’ shear stress mode. Haslach et al. (2018) observed that an aortic dissection, which started in the diseased part of the artery could also propagate further in the healthy tissue segment of the artery. The setup in this study was to execute a ring expansion test on a healthy aortic segment. The main advantage is a more physiological testing of the tissue than with conventional biaxial extension tests. The

specimens were prepared with an initial incision in the intima and during the experiment a dissection propagation was observed.

1.2.3. Numerical studies

Based on a cohesive zone model Gasser and Holzapfel (2006) introduced a nonlinear mechanical framework to investigate the three-dimensional properties of an arterial dissection for numerical simulations. With the consideration of the dispersion of the collagen fibers in the artery, the group expressed the dispersion with only one scalar parameter for the continuum. The cohesive part of the material problem aims to capture the dissection properties of the material, which includes the initialization and coalescence of micro-cracks into a discrete shape, where in the meantime the constitutive model was used to implement the structural information of the domain (Svensson and Crawford, 1992). Years later Ferrara and Pandolfi (2010) introduced a numerical model for an aortic dissection problem. Based on previous theories for fracture with cohesive models, they focused on the simulation of the delamination process in a multi-layer material.

Until the study of Noble et al. (2017) most studies focused on the propagation of a crack and neglected the formation of an initial tear. The focus of the study was on the creation of such an intimal tear. They investigated the cause of an initial tear originated by a stiff, planar penetrating external body (catheter-induced dissection) and formulate a model of the process using cohesive zone formulation.

1.2.4. Fracture mechanics

In the early twenties of the last century, Griffith (1920) attempted to solve fracture mechanical problems. As starting point, he selected the first law of thermodynamics and reformulated it to a simple energy balance equation to describe the theory of fracture evolution. He assumed that the growth of a crack would be sufficient to overcome the surface energy of a material, which further leads to a decrease of the stored strain energy in the material. This theory was exclusively valid for a fracture analysis of brittle material, until a modification in 1948, which introduced the local plastic flow of a material during tension was postulated (Irwin, 1948). Irwin (1956) developed the concept of the energy release rate based on previous studies from Griffith. In order to describe the stresses and the displacements close to a crack-tip by a single parameter, which was related to the energy release rate, Irwin introduced the so called stress intensity factor (Irwin, 1957). On the other side, there was another approach to characterize the nonlinear material behavior of a crack by Rice (1968). In this study, he was able to generalize the energy release rate of nonlinear materials by the idealization of the plastic deformation. Until Shih and Hutchinson (1976) provided a theoretical framework for the approach of Rice (1968), there was no fracture design analysis available for the case of linear elastic problems.

In recent studies, researchers are more focused to develop models based on the micro structure of the observed material. With this kind of modeling the crack behavior could

be related to the local and global material parameters. One of the more recent approaches for the modeling fracture of isotropic material is provided by Miehe et al. (2010). The aim of their study was to formulate a thermodynamically consistent crack phase-field model. In the same year the group introduced a rate-independent crack propagation based on an operator split (Miehe et al., 2010), to simplify the calculations of the system. Both of the previous mentioned approaches were based on the energy release of the Griffith theory (Griffith, 1920). Beside the strain energy release, other researchers focused on either the stress intensity factor (Irwin, 1957) or the crack tip plastic zone (Gasser and Holzapfel, 2006) theory for describing linear elastic fracture mechanics.

Based on the framework of Miehe et al. (2010), Gültekin et al. (2018) further introduced a structure tensor to model fracture of anisotropic materials, which represents the base of this study. Later Gültekin et al. (2017) extended the developed model (Gültekin et al., 2016) to model also finite strains, which was not considered in the model of Miehe et al. (2010).

2. Methods

This chapter gives an inside in the model for the rupture of an anisotropic material introduced by Gültekin et al. (2018) and it is based on a multi-field framework for fracture.

2.1. Multi-field framework for fracture

A continuum body $\mathcal{B} \subset \mathbb{R}^3$ can be described at time $t_0 \in \mathcal{T} \subset \mathbb{R}^+$ and $\mathcal{S} \subset \mathbb{R}^3$ at time $t \in \mathcal{T} \subset \mathbb{R}^+$ in an Euclidean coordinate system. To define this coupled problem of fracture two primary field variables are introduced, the bijective deformation map $\varphi(\mathbf{X}, t)$ and the internal variable for the crack phase-field d , i.e.

$$\varphi_t(\mathbf{X}) : \begin{cases} \mathcal{B} \times \mathcal{T} & \rightarrow \mathcal{S}, \\ (\mathbf{X}, t) & \mapsto \mathbf{x} = \varphi(\mathbf{X}, t), \end{cases} \quad d : \begin{cases} \mathcal{B} \times \mathcal{T} & \rightarrow [0, 1], \\ (\mathbf{X}, t) & \mapsto d(\mathbf{X}, t), \end{cases} \quad (2.1)$$

where $\varphi_t(\mathbf{X})$ maps a point $\mathbf{X} \in \mathcal{B}$ from the reference configuration to a point $\mathbf{x} \in \mathcal{S}$ in the current configuration, for a better understanding, see Fig. 2.1, and where d describes the thermodynamic approach to quantify fracture in a solid material, in general, it interpolates between the intact material ($d = 0$) and the ruptured state ($d = 1$), see Fig. 2.3. In comparison to the primary field variable $\varphi_t(\mathbf{X})$, which is defined in the current configuration, d is defined in the reference configuration.

2.1.1. Kinematics of mechanical problem

In this section the focus lies on the description of the mechanical problem of the multi-field framework, which is described with the primary field variable $\varphi_t(\mathbf{X})$, see Fig. 2.1. Since the variable $\varphi_t(\mathbf{X})$ is a coordinate system dependent parameter, it is recommended to work with the coordinate system independent invariants for implementation in a finite element method. The calculations below illustrate the method of obtaining these invariants of a continuum body \mathcal{S} in the current configuration. To reduce the cycle time of the code, the invariants are implemented in the Eulerian form, also called spatial description with respect to the spatial coordinates. Since $\varphi_t(\mathbf{X})$ describes a vector at a point in the continuum body, it is simpler to define a gradient which defines the changing of the deformation field, this is done by the calculation of the deformation gradient \mathbf{F} , i.e.

$$\mathbf{F} = \nabla \varphi_t(\mathbf{X}), \quad (2.2)$$

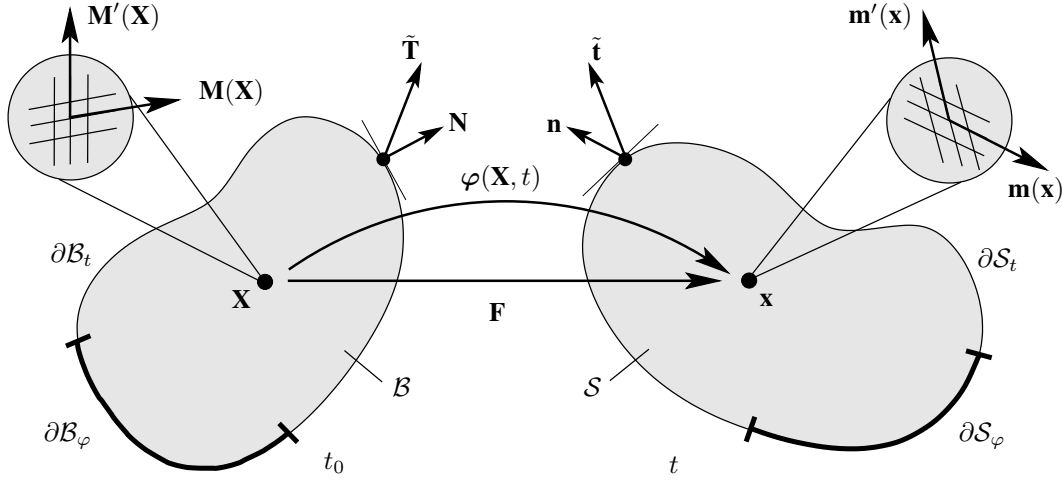


Figure 2.1.: Nonlinear deformation of an anisotropic continuum body with the material configuration of the body $\mathcal{B} \subset \mathbb{R}^3$ at t_0 and the current configuration $\mathcal{S} \subset \mathbb{R}^3$ at t . The surface of the body is described in the reference configuration by $\partial\mathcal{B}_\varphi \subset \mathbb{R}^2$ and analogous for the spatial configuration by $\partial\mathcal{S}_\varphi \subset \mathbb{R}^2$. $\tilde{\mathbf{T}}$, \mathbf{N} and $\tilde{\mathbf{t}}$, \mathbf{n} define the traction force and the normal vector on the surface of the body in the reference and spatial configuration, respectively in addition, the vectors $\mathbf{M}(\mathbf{X})$ and $\mathbf{M}'(\mathbf{X})$ represent the mean fiber direction of the anisotropic solid in the reference configuration and $\mathbf{m}(\mathbf{x})$ and $\mathbf{m}'(\mathbf{x})$ are specified for the directions in the spatial configuration. With the bijective deformation map $\varphi(\mathbf{X}, t)$ the deformation of a defined point \mathbf{X} in the reference configuration to a point \mathbf{x} in the spatial configuration can be defined over time. With permission from Gültekin et al. (2018).

where the operator ∇ defines the gradient of the deformation map $\varphi_t(\mathbf{X})$ in the material configuration. In the case of a volume change, from the reference configuration to the spatial configuration at different time steps, the variable J is further introduced. The variable $J(\mathbf{X}, t) = \det \mathbf{F}(\mathbf{X}, t)$ describes the volume ratio (or Jacobian matrix) from the spatial configuration of the continuum body \mathcal{S} related to the reference configuration of the body \mathcal{B} . Subject to the condition that it is not possible to reach a negative volume, the condition $J(\mathbf{X}, t) > 0$ has to be fulfilled at every time. In the case that $J(\mathbf{X}, t) = 1$ the volume behaves isochoric, also known as a volume-preserving deformation.

For the calculation of the stress response in a material, the strain of a material is an important measure, in spatial coordinates the deformation is defined with the matrix \mathbf{b} , also referred to as left Cauchy–Green tensor. Equation (2.3) shows the calculation of \mathbf{b} , i.e.

$$\mathbf{b} = \mathbf{F}\mathbf{G}^{-1}\mathbf{F}^T, \quad (2.3)$$

where \mathbf{G}^{-1} specifies the inverse of the co-variant reference metric tensor $\mathbf{G} = \delta_{IJ}\mathbf{E}^I \otimes \mathbf{E}^J$, where δ_{IJ} is the Kronecker delta function, which is equal to 1 only if the variables are equal otherwise it is 0. In general the tensor \mathbf{b} is symmetric and positive definite, i.e. that each eigenvalue is positive at each spatial coordinate \mathbf{x} . If a continuum body shows in each space

direction the same mechanical behavior, we say the material behaves isotropic. With this condition the stress response is not dependent on the choice of the operating coordinate system. To describe the stress response of an isotropic material, in general, only three invariants are needed, i.e.

$$I_1 = \text{tr} \mathbf{b}, \quad I_2 = \frac{1}{2} [I_1^2 - \text{tr}(\mathbf{b}^2)] \quad \text{and} \quad I_3 = \det \mathbf{b}. \quad (2.4)$$

To extend the isotropic material to a transversely isotropic material, with a preferred direction in the material, the structure tensors \mathbf{A}_m and $\mathbf{A}_{m'}$ are further introduced, i.e.

$$\mathbf{A}_m = \mathbf{m} \otimes \mathbf{m}, \quad \mathbf{A}_{m'} = \mathbf{m}' \otimes \mathbf{m}', \quad (2.5)$$

where $\mathbf{m}(\mathbf{x}) = \mathbf{FM}(\mathbf{X})$ and $\mathbf{m}'(\mathbf{x}) = \mathbf{FM}'(\mathbf{X})$ define the fiber directions in the deformed configuration. The physically significant fiber stretch related to anisotropic invariants I_4 and I_6 are defined by

$$I_4 = \mathbf{m} \cdot \mathbf{g} \mathbf{m} = \lambda^2, \quad I_6 = \mathbf{m}' \cdot \mathbf{g} \mathbf{m}' = \lambda^2, \quad (2.6)$$

with the co-variant spatial metric tensor $\mathbf{g} = \delta_{ij} \mathbf{e}^i \otimes \mathbf{e}^j$, where δ_{ij} defines again the Kronecker delta function, and λ^2 is the square of stretch of the fiber along its direction.

2.1.2. Geometrical approach for anisotropic rupture

In general, a phase-field is used to model a homogeneous material which undergoes a phase transition, this leads to a strong discontinuity in the continuum body \mathcal{B} . For the modeling of a crack exactly this kind of model is used to describe a fracture, which can also be seen as a discontinuity in a solid.

Crack phase-field in a one-dimensional bar

This section is for the general explanation of the crack phase-field, in the next section the crack phase-field is expanded to a three-dimensional domain. To describe the basic principles of the crack phase-field a continuum body \mathcal{B} was assumed to describe an infinite long beam with the cross-section Γ and a length $L = [-\infty, \infty]$. For an implementation of a crack the position $x \in L$ along the x -axis is further defined. In the event of a sharp crack, which is defined as a strong discontinuity in the domain, it is assumed that the crack manifests itself as a jump of the internal field variable d to the value 1. Figure 2.2(a) shows the change of the field variable d for the case of a sharp crack, where it is assumed that the crack appears at the position $x = 0$. Since it is assumed to be a sharp crack the material next to this location will remain intact and the value for d stays at 0. For the numerical analysis of a domain with a sharp crack, this represents a major complexity (Fig. 2.2(a)). To simplify this problem the jump of the internal field variable d has to be smoothed out, seen in Fig. 2.2(b). For the smoother transition between the intact and the ruptured state,

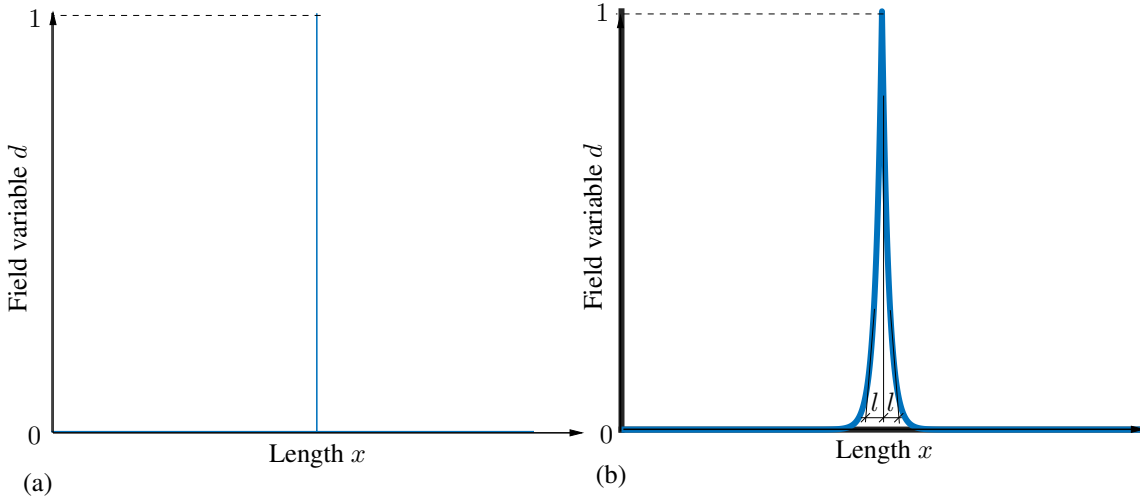


Figure 2.2.: Sharp and diffusive crack modeling: (a) sharp crack at $x = 0$, defined by a strong discontinuity in regard to the internal field variable d to 1; (b) diffusive crack at $x = 0$ with length scaling factor l , for a smoothing out by the function $d(x) = e^{-|x|/l}$ of the crack along the x -axis of an infinite bar.

an exponential function is used to approximate the transition between both states, Miehe et al. (2010) used an exponential function as

$$d(x) = e^{-\frac{|x|}{l}}, \quad (2.7)$$

where l defines the length scale of the diffusive crack over the domain L of the bar for their study. Based on this condition a functional $\Gamma_l(d)$ was introduced in the same study, i.e.

$$\Gamma_l(d) := \frac{1}{l}I(d) = \frac{1}{2l} \int_{\mathcal{B}} (d^2 + l^2 d'^2) dV, \quad (2.8)$$

where $I(d)$ is a developed functional of a homogeneous differential equation to describe a diffusive crack surface. With the introduction of $I(d)$ to describe the crack surface, a constitutive model for fracture mechanical problems can be developed in the next step.

Crack phase-field in a continuum body

This section explains the application of a crack phase-field on a continuous formulation and extends the one-dimensional approach from the previous section to a multi-dimensional domain, seen in Fig. 2.3. In Fig. 2.3, Γ is defined as a strong discontinuous boundary of a sharp crack in the continuum body \mathcal{B} with the dimension $\Gamma \in \partial\mathcal{B}_\varphi \subset \mathbb{R}^2$ at reference time t_0 , i.e. $\Gamma = \int_{\Gamma} dA$, which is denoted by a solid black line. To generate an overall continuous domain of this problem, the crack will be approximated over the volume and leads further to a regularized crack surface $\Gamma_l(d)$, i.e.

$$\Gamma_l(d) = \int_{\mathcal{B}} \gamma(d, \nabla d) dV, \quad \gamma(d, \nabla d) = \frac{1}{2l} (d^2 + l^2 \nabla d \cdot \nabla d), \quad (2.9)$$

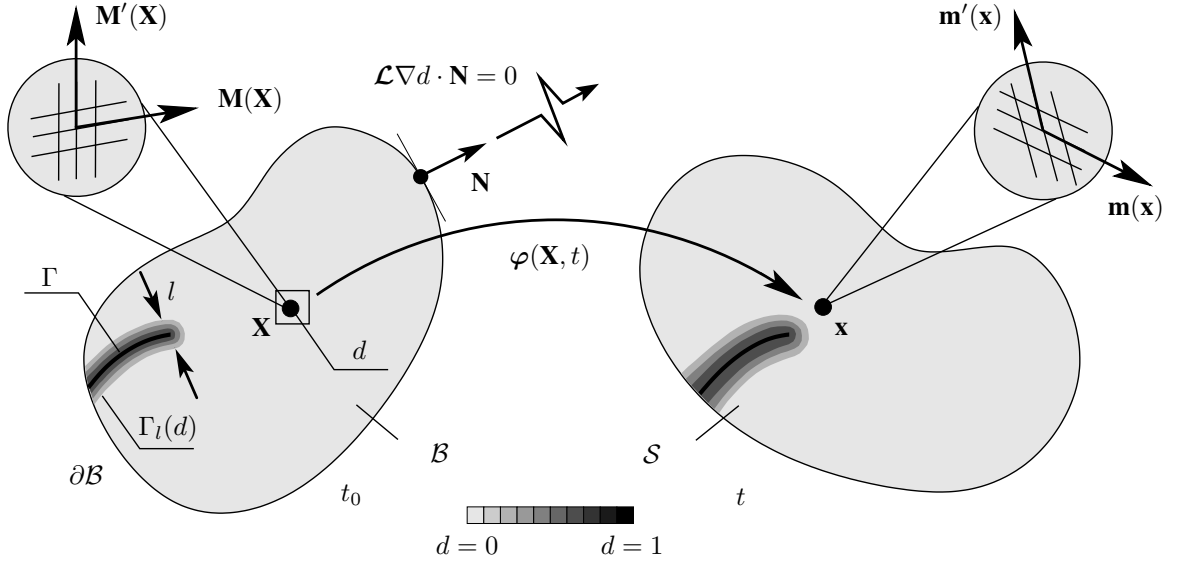


Figure 2.3.: Overview of a continuum body with a sharp crack surface Γ and a diffusive crack surface $\Gamma_l(d)$ in the material configuration $\mathcal{B} \subset \mathbb{R}^3$ and the current configuration $\mathcal{S} \subset \mathbb{R}^3$, respectively where the diffusive crack surface is regularized by the length-scale l . The fiber directions are given by $\mathbf{M}(\mathbf{X})$ and $\mathbf{M}'(\mathbf{X})$ for the reference configuration and by parameter $\mathbf{m}(\mathbf{x})$ and the parameter $\mathbf{m}'(\mathbf{x})$ as the spatial counterparts. The anisotropic crack phase-field is further specified by a Neumann-type boundary condition, which leads to a traction-free continuum body $\mathcal{L}\nabla d \cdot \mathbf{N} = 0$. With permission from Gültekin et al. (2018).

where $\gamma(d, \nabla d)$ describes the isotropic crack surface density function. This approach from Miehe et al. (2010) was then extended by Gültekin et al. (2018) for an anisotropic material with the anisotropic structure tensor \mathcal{L} such that

$$\Gamma_l(d) = \int_{\mathcal{B}} \gamma(d, \nabla d; \mathcal{L}) dV, \quad \text{where} \quad \gamma(d, \nabla d; \mathcal{L}) = \frac{1}{2l} (d^2 + \nabla d \cdot \mathcal{L} \nabla d), \quad (2.10)$$

describes the crack surface with an anisotropic crack surface density function. In the model of Gültekin et al. (2018) the second-order tensor \mathcal{L} is defined as

$$\mathcal{L} = l^2 [\mathbf{I} + \omega_M \mathbf{M} \otimes \mathbf{M} + \omega_{M'} \mathbf{M}' \otimes \mathbf{M}'], \quad (2.11)$$

where the parameters ω_M and $\omega_{M'}$ are defined as penalty terms, in other words, weighting terms, for the anisotropy in certain fiber direction. To ensure stability of the simulation the variable ω_i with $i \in \{M, M'\}$ is limited to the open range $-1 < \omega_i < \infty$.

2.2. Strong form of the multi-field problem

With the characterization of the multi-field problem it is possible to obtain a representative model for fracture in an anisotropic material. As a starting point the rate-type of the

potential energy density Π_η was used, i.e.

$$\Pi_\eta = \mathcal{E} + \mathcal{D}_\eta - \mathcal{P}, \quad (2.12)$$

where \mathcal{E} characterizes the rate of energy storage functional in the material, \mathcal{D}_η specifies the viscous regularized dissipation functional due to fracture and \mathcal{P} characterizes the external power functional on the observed domain.

The following passage is devoted to the calculation of the rate of energy storage functional $\mathcal{E}(\dot{\varphi}; \dot{d})$ in the material, and is defined by

$$\mathcal{E}(\dot{\varphi}; \dot{d}) = \int_B (\boldsymbol{\tau} : \mathbf{g} \nabla_x \dot{\varphi} - f \dot{d}) dV, \quad (2.13)$$

with the variables φ and d , which are work conjugated to the Kirchhoff stress tensor $\boldsymbol{\tau}$ and the thermodynamic force f , where $\boldsymbol{\tau}$ is simply calculated with the push forward applied to \mathbf{S} ($\boldsymbol{\tau} = \mathbf{F} \mathbf{S} \mathbf{F}^T$). The thermodynamic force f governs the damage evolution.

Thus,

$$\boldsymbol{\tau} := 2\partial_{\mathbf{g}} \Psi(\mathbf{g}, \mathbf{F}, \mathbf{A}_m, \mathbf{A}_{m'}; d), \quad f := -\partial_d \Psi(\mathbf{g}, \mathbf{F}, \mathbf{A}_m, \mathbf{A}_{m'}; d). \quad (2.14)$$

Based on the developed fracture criterion by Griffith (1920) $\mathcal{E}(\dot{\varphi}; \dot{d})$ also includes the consideration of degradation due to fracture. This mechanical degradation is modeled by the use of the function g_i with $i = \{\text{ani}, \text{iso}\}$ for the isotropic and anisotropic material behavior, i.e.

$$g_{\text{iso}}(d) = (1 - d)^{a_{\text{iso}}} \quad \text{and} \quad g_{\text{ani}}(d) = (1 - d)^{a_{\text{ani}}}, \quad (2.15)$$

where a_i , $i \in \{\text{ani}, \text{iso}\}$, controls the rate of mechanical degradation. For simplification of the model the defined parameter from Miehe et al. (2010) were used ($a_{\text{iso}} = 2$ and $a_{\text{ani}} = 2$), as shown in Fig. 2.4. To ensure a monotonic mechanical degradation the form

$$g'_i(d) \leq 0 \quad \text{with} \quad g_i(0) = 1, \quad g_i(1) = 0, \quad g'_i(1) = 0, \quad (2.16)$$

is used. The second and third conditions are used to define the limits of the ruptured and intact state of the material, and the last term ensures the saturation of $g_i(d)$ in the fully ruptured state. In the model of Gültekin et al. (2018) the stored energy in the intact ($d = 0$) material is defined in the form

$$\Psi_0(\mathbf{g}, \mathbf{F}, J, \mathbf{A}_m, \mathbf{A}_{m'}) = \Psi_0^{\text{iso}}(\mathbf{g}, \mathbf{F}, J) + \Psi_0^{\text{ani}}(\mathbf{g}, \mathbf{F}, \mathbf{A}_m, \mathbf{A}_{m'}), \quad (2.17)$$

where $\Psi_0^{\text{iso}}(\mathbf{g}, \mathbf{F}, J)$ and $\Psi_0^{\text{ani}}(\mathbf{g}, \mathbf{F}, \mathbf{A}_m)$ refers to the isotropic and anisotropic parts of the Helmholtz free-energy function without fracture respectively. They are defined as

$$\Psi_0^{\text{iso}}(\mathbf{g}, \mathbf{F}, J) = \hat{\Psi}_0^{\text{iso}}(J, I_1) \quad \text{and} \quad \Psi_0^{\text{ani}}(\mathbf{g}, \mathbf{F}, \mathbf{A}_m, \mathbf{A}_{m'}) = \hat{\Psi}_0^{\text{ani}}(I_4, I_6). \quad (2.18)$$

For a more detailed formulation of the Helmholtz free-energy function Ψ and how the formulations are implemented in a finite element code, see Appendix A, which shows the

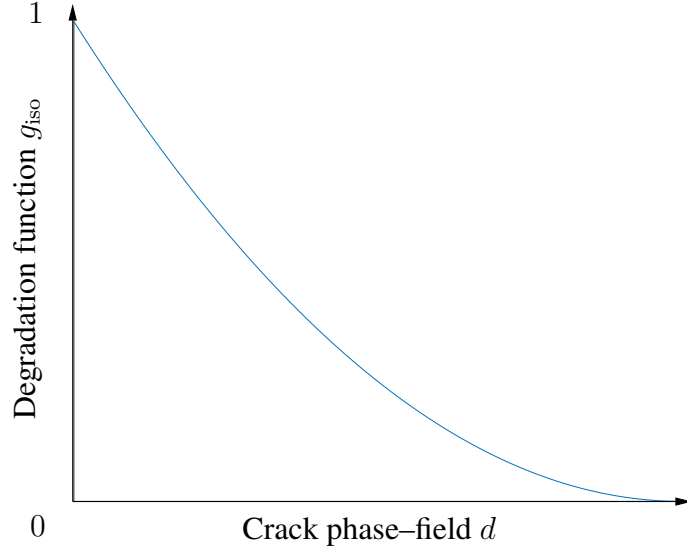


Figure 2.4.: Mechanical degradation function $g_i(d)$, $i \in \{\text{iso}, \text{ani}\}$, in regard to an increase of the internal field variable d , which represents the rupture state of the material.

case for an incompressible material. With the usage of the degradation functions $g_{\text{iso}}(d)$ and $g_{\text{ani}}(d)$ it is possible to end up with the Helmholtz free–energy function Ψ with respect to the crack phase–field d and the degradation function $g_i(d)$, $i \in \{\text{iso}, \text{ani}\}$, i.e.

$$\Psi(\mathbf{g}, \mathbf{F}, J, \mathbf{A}_{\mathbf{m}}, \mathbf{A}_{\mathbf{m}'}; d) = g_{\text{iso}}(d)\Psi_0^{\text{iso}}(\mathbf{g}, \mathbf{F}, J) + g_{\text{ani}}(d)\Psi_0^{\text{ani}}(\mathbf{g}, \mathbf{F}, \mathbf{A}_{\mathbf{m}}, \mathbf{A}_{\mathbf{m}'}). \quad (2.19)$$

The second term on the right–hand side of Eq. (2.12) defines the viscous regularized dissipation functional. The parameter η classifies the artificial viscosity of the continuum body, which is used as a stabilization parameter for crack simulation. Accordingly, to a correct crack propagation, $\eta \geq 0$ should be assumed to be positive and close to 0, i.e.

$$\mathcal{D}_\eta(\dot{d}, \beta; d) = \int_{\mathcal{B}} \left[\beta \dot{d} - \frac{1}{2\eta} \langle \chi(\beta; d, \nabla d) \rangle^2 \right] dV, \quad (2.20)$$

where β defines the local driving force, \dot{d} describes the rate of the deformation tensor and χ , for which the Macaulay brackets $\langle \bullet \rangle = [(\bullet) + |(\bullet)|]/2$ is defined to filter out the positive values from the argument ($\chi > 0$), defines the scalar viscous over–stress term, i.e.

$$\chi(\beta; d, \nabla d) = \beta - g_c[\delta_d \gamma(d, \nabla d; \mathcal{L})], \quad (2.21)$$

where the parameter g_c defines the related variable to the critical fracture energy.

The last term in Eq. (2.12) on the right–hand side refers to the external power functional $\mathcal{P}(\dot{\varphi})$ which is defined by

$$\mathcal{P}(\dot{\varphi}) = \int_{\mathcal{B}} \rho_0 \tilde{\gamma} \cdot \dot{\varphi} dV + \int_{\partial \mathcal{B}_t} \tilde{\mathbf{t}} \cdot \dot{\varphi} da, \quad (2.22)$$

where ρ_0 , $\tilde{\gamma}$ and $\tilde{\mathbf{t}}$ define the material density, the described spatial body force and the spatial surface traction, respectively.

Finally, with the rate-dependent potential Π_η , it is possible to propose a mixed variational principle of the evolution problem according to

$$\{\dot{\varphi}, \dot{d}, \beta\} = \text{Arg} \left\{ \inf_{\dot{\varphi} \in \mathcal{W}_{\dot{\varphi}}} \inf_{d \in \mathcal{W}_d} \sup_{\beta \geq 0} \Pi_\eta \right\}, \quad (2.23)$$

where the defined domains for the field variables $\dot{\varphi}$ and \dot{d} are

$$\mathcal{W}_{\dot{\varphi}} = \{\dot{\varphi} \mid \dot{\varphi} = \mathbf{0} \quad \text{on} \quad \partial\mathcal{B}_\varphi\}, \quad \mathcal{W}_d = \{\dot{d} \mid \dot{d} = 0 \quad \text{on} \quad \partial\mathcal{B}_d\}. \quad (2.24)$$

After the variation of Π_η regarding to the fields of $\{\dot{\varphi}, \dot{d}, \beta\}$, and additional mathematical manipulations, Gültekin et al. (2018) introduced two main considerations for modeling rupture.

The first consideration describes the balance of linear momentum in a continuum body, i.e.

$$\boxed{1: J \operatorname{div}(J^{-1}\boldsymbol{\tau}) + \rho_0 \tilde{\gamma} = \mathbf{0}.} \quad (2.25)$$

The characterization of the rate-dependent evolution of the crack phase-field, is

$$\boxed{2: \eta \dot{d} = 2(1-d)\overline{\mathcal{H}} - d + \operatorname{Div}(\mathcal{L}\nabla d),} \quad (2.26)$$

where the first term of the right-hand side defines the driving force of the fracture with respect to the dimensionless crack driving source term $\overline{\mathcal{H}}$, and the second term specifies the geometric resistance of the material with respect to the second-order structure tensor \mathcal{L} . The crack driving source term can be described with

$$\overline{\mathcal{H}} = \frac{\Psi_0}{g_c/l}, \quad (2.27)$$

where Ψ_0 and g_c define the effective free-energy function and the critical energy release rate in the continuum body. To define the contribution of the isotropic ground matrix and the anisotropic fibers in the continuum the quantity $\overline{\mathcal{H}}$ is decoupled in the respective terms

$$\overline{\mathcal{H}} = \overline{\mathcal{H}}^{\text{iso}} + \overline{\mathcal{H}}^{\text{ani}}, \quad (2.28)$$

with

$$\overline{\mathcal{H}}^{\text{iso}} = \frac{\Psi_0^{\text{iso}}}{g_c^{\text{iso}}/l}, \quad \overline{\mathcal{H}}^{\text{ani}} = \frac{\Psi_0^{\text{ani}}}{g_c^{\text{ani}}/l}. \quad (2.29)$$

These terms will be regulated by the length-scale regularized parameter g_c^i with $i \in \{\text{iso}, \text{ani}\}$. For more details please refer to Griffith (1920), which introduced g_c as a parameter of fracture, defining the fracture toughness of a material. The fundamental criterion for fracture in this model is based on the energy criterion and based on the energy release rate g , which defines the change of the potential energy in the crack region, in the case of $g < g_c$, the

energy release rate g in the domain is below the threshold value g_c and does not lead to fracture (Anderson, 2005). In the event $g = g_c$, a crack can start to propagate through a linear elastic material domain (Anderson, 2005). To specify a rate-independent case for the crack evolution $\eta \rightarrow 0$, Eq. (2.26) can be reformulated in a crack evolution equation for the isotropic and anisotropic crack driving source term, i.e.

$$\begin{aligned} 2(1-d)\overline{\mathcal{H}}^{\text{iso}} &= d - \text{Div}(\mathcal{L}^{\text{iso}}\nabla d), \\ 2(1-d)\overline{\mathcal{H}}^{\text{ani}} &= d - \text{Div}(\mathcal{L}^{\text{ani}}\nabla d), \end{aligned} \quad (2.30)$$

where \mathcal{L}^{iso} represents the part of the second-order structure tensor related to the isotropic ground matrix and \mathcal{L}^{ani} defines the contribution to \mathcal{L} from the fibers, with the definition

$$\mathcal{L}^{\text{iso}} = l^2 \mathbf{I} \quad \text{and} \quad \mathcal{L}^{\text{ani}} = l^2 [\omega_{\mathbf{M}} \mathbf{M} \otimes \mathbf{M} + \omega_{\mathbf{M}'} \mathbf{M}' \otimes \mathbf{M}']. \quad (2.31)$$

These relations are interpolated in Eq. (2.26), which leads to

$$(1-d)\mathcal{H} = d - \frac{1}{2} \text{Div}(\mathcal{L}\nabla d), \quad (2.32)$$

where \mathcal{H} defines the maximal value of the crack driving source term in the deformation history $\overline{\mathcal{H}}(s)$, $s \in \{0, t\}$, with the restriction to an irreversible and positive crack driving source term \mathcal{H} for the fracture propagation. This characteristic is ensured with the use of the Macaulay brackets, where the positive values are filtered out, i.e.

$$\mathcal{H}(t) = \max_{s \in [0, t]} [\langle \overline{\mathcal{H}}(s) - 1 \rangle], \quad (2.33)$$

where $\overline{\mathcal{H}}(s) - 1$ keeps the domain intact until the failure surface is reached and it assures a fracture zone without the ability for self healing. With this it is possible to reformulate the strong form of the crack evolution equation (Eq. (2.26)) to the following expression

$$\boxed{\underbrace{\eta \dot{d}}_{\text{crack evolution}} = \underbrace{(1-d)\mathcal{H}}_{\text{driving force}} - \underbrace{\left[d - \frac{1}{2} \text{Div}(\mathcal{L}\nabla d) \right]}_{\text{geometric resistance}}}. \quad (2.34)$$

With this assumption, for the strong forms (2.25) and (2.34), it is feasible to generate a discrete weak formulation for the temporal and the spatial space, a general approach for that is shown in the Appendix B.

3. Results

For the validation of the model it is important to identify the material parameters, which was performed by, e.g., Sommer et al. (2016). In the next step, the model was applied to a generated mesh by the program CUBIT[®] Release (2017), and it was further called by the input file of the finite element analysis program FEAP[®] Release (2008). With this package the analysis of the sensitivity in regard to ω_M and an aortic dissection boundary-value problem were investigated.

3.1. Parameter identification

The parameter identification is based on the testing protocol of Sommer et al. (2016). In this study, the authors used uniaxial extension tests and in-plane simple shear tests to obtain material parameters for aneurysmatic and dissected medial tissue strips. They performed uniaxial extension tests along the circumferential θ - and the longitudinal z -directions, defined as $(\theta\theta)$ and (zz) modes. For the characterization of the in-plane simple shear response, the experiments were executed by facing the radial plane r and along the θ - and z -direction, which are represented by the modes $(r\theta)$ and (rz) , see Fig. 3.1. The least-squares method was applied to a nonlinear objective function $\chi^2(\mathbf{p})$ to estimate the unknown parameters related to the elastic material parameters $\mathbf{p} = \{\mu, k_1, k_2, \alpha\}$ of the constitutive model by Holzapfel et al. (2000). An efficient estimation for these parameters is successfully obtained when a minimum of variance between the objective function and the experimental data is achieved, i.e.

$$\min_{\mathbf{p}} \chi^2(\mathbf{p}) = \sum_{(ij) \in \mathbf{m}} \sum_{n=1}^{N_{\text{exp}}^{(ij)}} (\sigma_{(ij)}^n - \bar{\sigma}_{(ij)}^n)^2, \quad (3.1)$$

where $\sigma_{(ij)}^n$ describes the model-predicted Cauchy stress and $\bar{\sigma}_{(ij)}^n$ defines the experimentally achieved Cauchy stress. Equation (3.1) was further executed for the different mode types of uniaxial extension and in-plane simple shear, with $\mathbf{m} = \{(\theta\theta), (zz), (r\theta), (rz)\}$ for the different loading scenarios at special data points $N_{\text{exp}}^{(ij)}$ during an experiment. To solve the minimization problem (3.1) and to obtain the optimized parameters for the system, the Euclidean norm was calculated by the built-in MATLAB[®] Release (2016b) function `lsqnonlin`. The outcome of the optimization process is summarized in Table 3.1. For the validation of the fitting, a linear correlation coefficient $R_{(ij)}^2$ and the root-mean-square

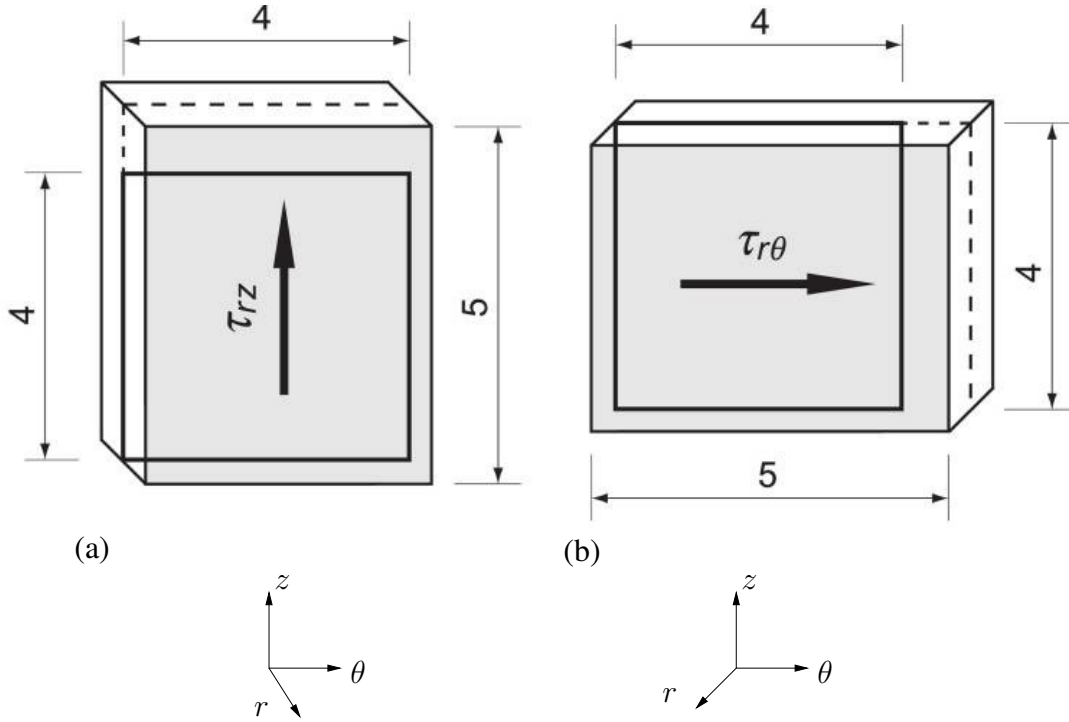


Figure 3.1.: Schematics of an ‘in–plane’ shear testing sample: (a) applied shear in the longitudinal direction τ_{rz} ; (b) applied shear in circumferential direction $\tau_{r\theta}$ to extract the shear responds of the $z\theta$ –plane. Gray surfaces show the fixated surfaces and the dashed lines, represent incisions of approximately 1[mm]. With permission from Sommer et al. (2016).

error ϵ was defined as

$$\epsilon = \frac{\sqrt{\frac{\chi^2(\mathbf{p})}{\sum_{(ij) \in \mathbf{m}} N_{\text{exp}}^{(ij)} - q}}}{\sum_{(ij) \in \mathbf{m}} \bar{\sigma}_{(ij)}^{\text{mean}}}, \quad (3.2)$$

where q is defined as the number of fitting parameters \mathbf{p} and $\bar{\sigma}_{(ij)}^{\text{mean}}$ specifies the arithmetic mean of the mode related Cauchy stresses, see also Holzapfel et al. (2005) and Schulze–Bauer et al. (2003).

Note, that in the case of a complete correlation $R_{(ij)}^2 = 1$, the ‘goodness of fit’ reaches its maximum, which leads to the estimation of the parameters \mathbf{p} related to the specific mode. Figure 3.2 illustrates the different modes of loading of a medial sample strip. The ‘Experiment’ curve is defined by the results of the experimental data points of the different loading modes. Furthermore, the term ‘Model’ indicates the elastic material response of the proposed model (Gültekin et al., 2017) before rupture occurs, and ‘FEM’ is the Cauchy stress related to the constitutive model of Holzapfel et al. (2000) without considering any

Table 3.1.: Elastic material parameters obtained with the nonlinear least–squares method, correlation coefficients and root–mean–square error.

	μ [kPa]	k_1 [kPa]	k_2 [-]	α [°]
Elastic material parameters	83.51	101.65	4.17	44.71
Correlation coefficients	$R^2_{(r\theta)} = 0.99$	$R^2_{(rz)} = 0.98$	$R^2_{(\theta\theta)} = 0.98$	$R^2_{(zz)} = 0.99$
Root–mean–square error	$\epsilon = 0.1043$			

damage. In Fig. 3.2 it is shown that the assumption of an hyperelastic model response is acceptable.

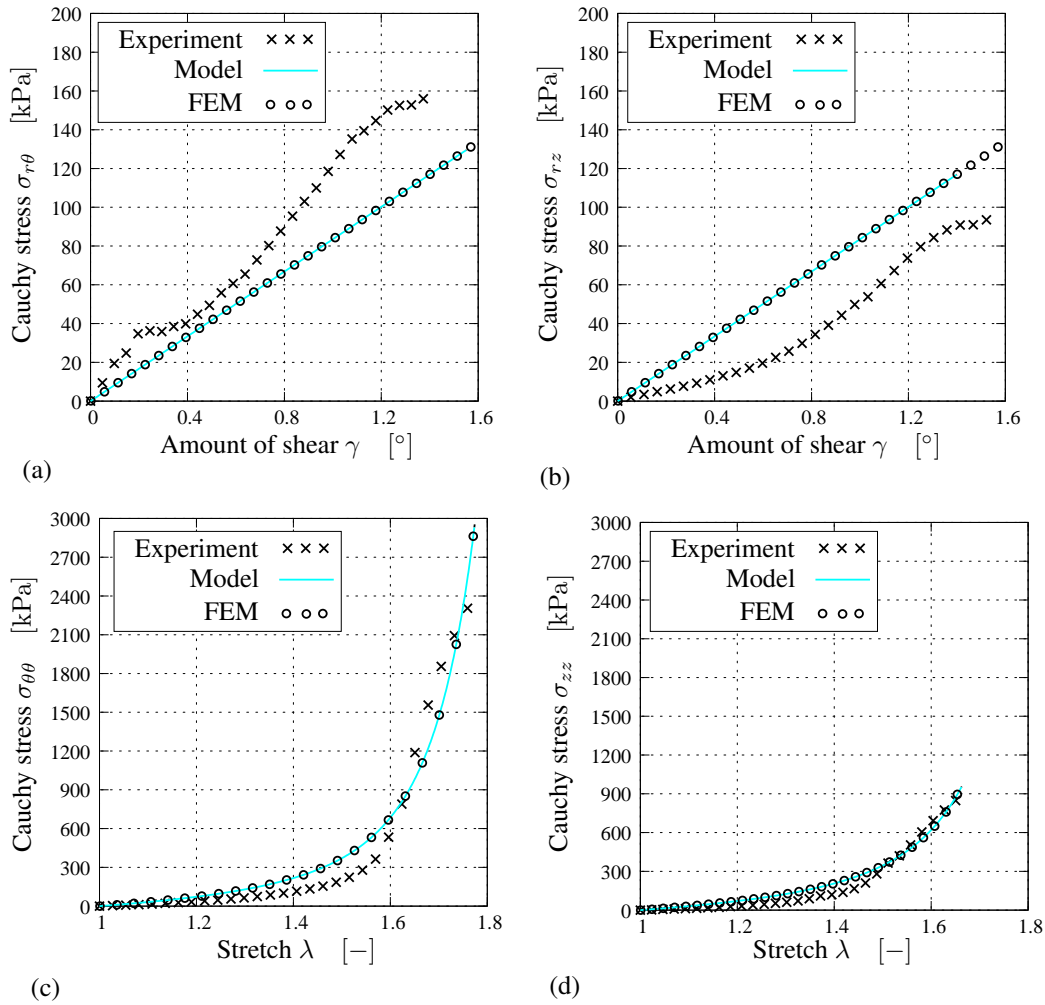


Figure 3.2.: In-plane simple shear and uniaxial extension test data corresponding to the model (Gültekin et al., 2017) and the hyperelastic FEAP[®] Release (2008) model for (a) ($r\theta$); (b) (rz); (c) ($\theta\theta$); (d) (zz) modes.

3.2. Parameter validation of the healthy medial sub-layer

Due to the lack of mechanical material parameters for healthy medial sub-layers (Sommer et al., 2016) the stress on the interface of a healthy medial sub-layer and a degenerated medial sub-layer remains unclear. For that reason an additional investigation regarding the mechanical stress concentration on the interface of these two sub-layers was executed. As an initial consideration we assumed that the cross-links between two fibers are the main cause of fracture propagation along the aorta. To show this assumption for the mechanical response an in-plane simple shear test was executed on a specimen, which consists of two medial sub-layers. The investigated domain considered a healthy medial sub-layer with increased parameters with respect to the parameters of the degenerated medial sub-layer. Figure 3.3 shows the structure of the domain, where the healthy sub-layer is represented by the cyan-colored layer and an attached degenerated medial sub-layer (pink-color) is on the top.

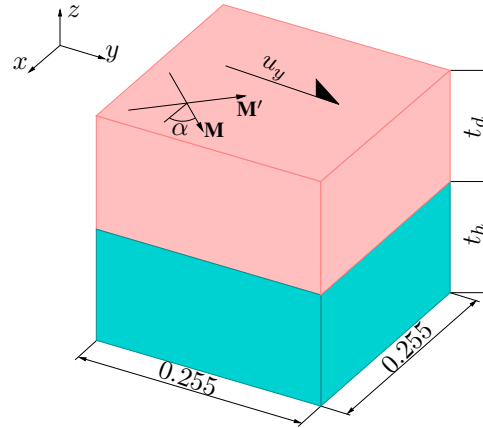


Figure 3.3.: Geometry for the analysis of the stress concentration at the interface of two medial sub-layers, where the pink-layer visualizes a degenerated medial sub-layer with the defined material parameters (see Table 3.1) and with the thickness $t_d = 0.1275$ [mm], while the healthy sub-layer (thickness $t_h = 0.1275$ [mm]) is represented by the cyan-colored sheet. The boundary condition of the domain was assumed to be zero at the top-surface ($z = 0.255$) and the bottom-surface ($z = 0$), which means a restriction against the deformation of these surfaces. \mathbf{M} and \mathbf{M}' represent the mean fiber directions for both fiber families, where the angle $\alpha = 45[^\circ]$ is defined as the angle of the first fiber family with respect to the x -axis. Applied on the top-surface, the in-plane simple shear is defined by u_y in the y -direction. All dimensions are given in [mm].

The thickness of these layers (t_h and t_d), defined in the z -direction, was adjusted to the thickness of a single medial sub-layer (Ross and Pawlina, 2011). For the remaining measurements of the strip, arbitrary values were considered. The simulation considered that both fiber families are active and defined by their mean fiber direction \mathbf{M} and \mathbf{M}' . For the elastic material parameters, the values from Section 3.1 were used to characterize the mechanical properties of the degenerated medial sub-layer (see Table 3.1). In contrast

to these parameters the material parameters k_1 and k_2 were increased by 20 % related to the values of the degenerated sub-layer. For the shear-modulus two different values were assumed (2- or 10-times higher than for the degenerated sheet) to investigate the stress on the interface surface with respect to a change of the stiffness of the healthy sheet, summarized in Tabel 3.2. Note that in both sheets the value for α , the angle between the first fiber family and the x -axis remains equal. The discrete domain is further composed

Table 3.2.: Material parameters for the analysis of the stress concentration with different stiffnesses, for the healthy medial sub-layer with respect to the properties of the degenerated medial sub-layer.

	μ [kPa]	k_1 [kPa]	k_2 [-]	α [°]
Degenerated elastic material parameters	83.5	101.65	4.17	44.7
Healthy elastic material parameters (1)	167.01	121.98	5.00	44.7
Healthy elastic material parameters (2)	835.08	121.98	5.00	44.7

of 2366 hexahedral elements with a total amount of 2940 nodes over the domain. Since the aim of this investigation is to obtain the stress concentration at the interface of the two sub-layers, only the hyperelastic part of the described model is used and the crack phase-field term is disregarded.

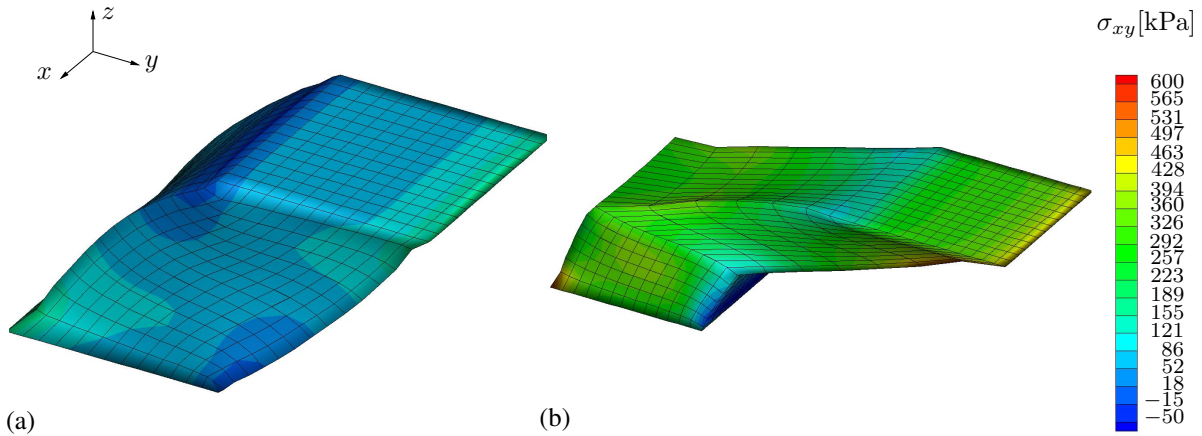


Figure 3.4.: Stress distribution on the surface of the domain caused by a shear deformation along the y -direction, where the load was applied on the top-surface ($z = 0.255$ [mm]), with (a) 100%, and (b) 500% increased stiffness for the healthy sub-layer related to the degenerated sub-layer. The domain is visualized in Eulerian configuration.

Figure 3.4(a) represents the Cauchy stress σ_{xy} [kPa] on the surface of the chosen domain, where the elastic parameters for the healthy medial sub-layer are assumed to be two times higher than the parameters for the degenerated sub-layer, with a stretch λ [-] along the y -direction. It can also be observed, that the stress in Fig. 3.4(a) is significantly lower than the

stress in Fig. 3.4(b), with 5 times higher shear–modulus compared to (a). It is also clearly visible, that with a smaller difference between the elastic parameters of the degenerated layer and the healthy layer the finite elements are less deformed (see Fig. 3.4(a)) than with a higher mechanical parameter. For further investigation of the stresses on the interface surface, the provided Slices–function of the program Tecplot[®] 360 (2017) was used to generate Fig. 3.5. In contrast to Fig. 3.4, which uses the Eulerian coordinates for the visualization of the domain, Fig. 3.5 shows the Cauchy stress σ_{xy} [kPa] of the interface region in the Lagrangian configuration.

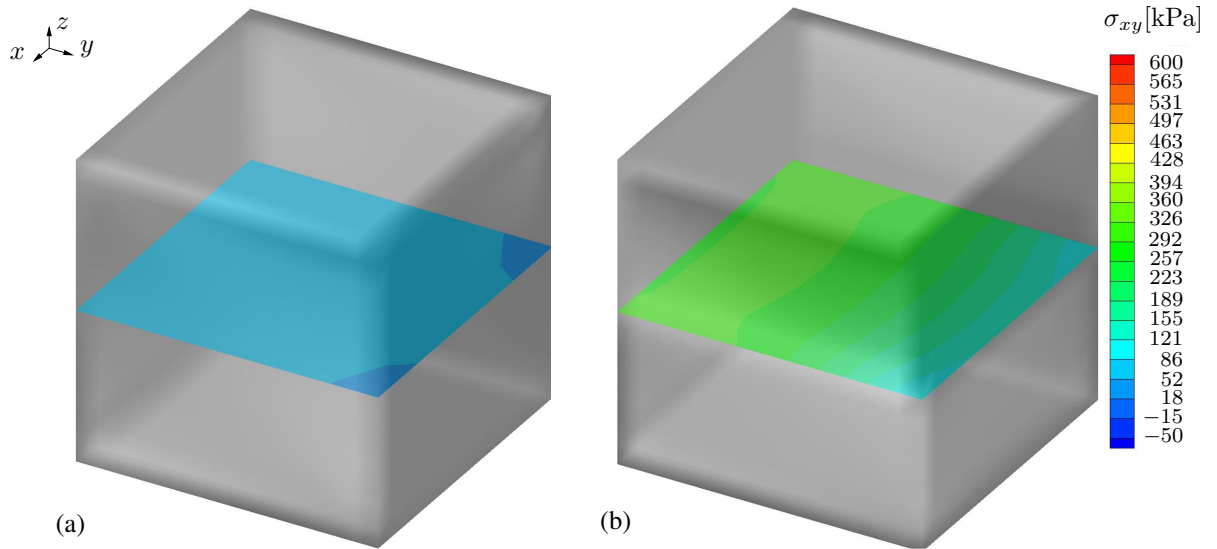


Figure 3.5.: Cauchy stress distribution investigated on the interface surface of two sub–layers, with (a) 100 %, and (b) 500 % increased stiffnesses for the healthy sub–layer related to the degenerated sub–layer and an applied shear load on the top–surface of the domain along the y –direction. The domain is visualized in Lagrangian configuration.

In Fig. 3.5(a) it can be seen that the right edges of the domain show lower stress values caused by the applied shear load along the y –direction. Compared to the twice higher stiffness parameters, Fig. 3.5(b) shows the stress values for a ten times higher shear–modulus of the healthy medial sub–layer, and the same elastic parameters as the 100% stiffer medial layer. As can be seen the Cauchy stress σ_{xy} [kPa] in the x – y –plane is significantly higher than the stress in the same plane with the lower shear–modulus (see Fig. 3.5(a)). For more details of the stress on the interface between the two sub–layers, the resulting stresses at node # 217 (node in the middle of the interface surface) are visualized in Fig. 3.6.

In this figure the cyan–colored curve represents a composite of a degenerated medial sub–layer with an attached healthy sub–layer sheet, the parameter sets are listed in Table 3.2 (degenerated– or healthy elastic material parameters (1)). In contrast, the red curve shows the Cauchy stress trend in a composite with the material parameters from Table 3.2, where the healthy sheet parameters were assumed to be the healthy elastic material param–

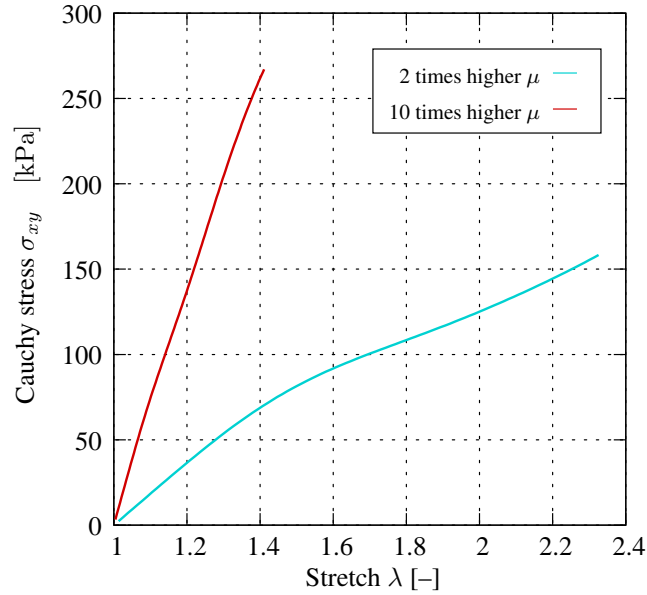


Figure 3.6.: Stress–stretch curves for a domain composed of a degenerated and a healthy medial sub–layer, where the contrast of these layers is defined by the different stiffness parameters and in addition with two different shear–moduli for the healthy medial sub–layer. The cyan–colored curve represents an assembly of a degenerated medial sub–layer with the defined parameters (see Table 3.2) and a medial sub–layer with two times higher parameters. Compared to the cyan–colored curve the red–colored curve shows the Cauchy stress values for the same parameters for the medial sub–layer related to a stiffer sub–layer .

eters (2). Despite the fact that both domains underwent the same shear–load the stretch λ at node # 217 is significant higher than on the same element node in the other material composite with a ten times higher shear–modulus μ . In addition, an increase of the shear–modulus μ in the healthy medial sub–layer causes an enhancement of the Cauchy stress. With this in mind the parameters for the following study, where the elastic material parameters are chosen to be 20% higher for the healthy sub–layers as the material parameters for the degenerated sub–layer, an initiation of a fracture can not really be observed. Based on this investigation, a more precise determination of the elastic parameters through further experimental studies is necessary in order to observe a failure criterion which causes a delamination between the two sheets.

3.3. Sensitivity of a crack path related to the anisotropy in the material

To investigate the dependency of the crack path on the anisotropy parameters ω_M and $\omega_{M'}$ an uniaxial extension load was applied on a single–edge–notched plate, see Fig. 3.7. The domain was fixed at the bottom edge in the x and y directions, defined as $u_0 = 0$, and at the top edge a linear increasing load was applied, which leads to a displacement of the upper boundary by u_y . To simplify the boundary–value problem, one fiber direction was assumed, with the angle $\alpha = 45[^\circ]$ related to the x –axis, and defined by the mean fiber vector \mathbf{M} .

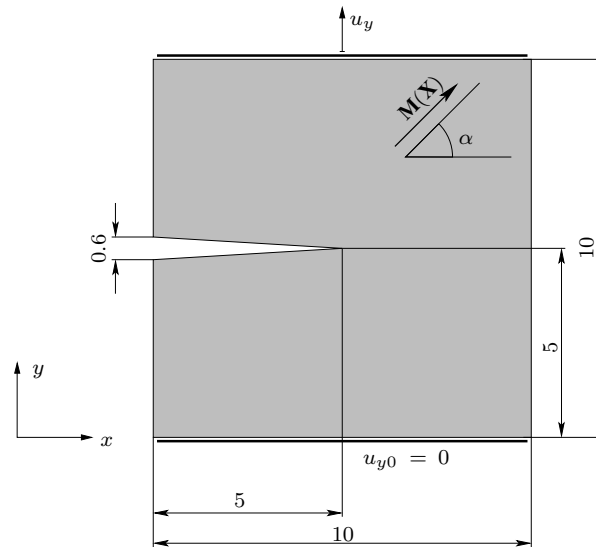


Figure 3.7.: Geometry of a single–edge–notched plate boundary–value problem for the sensitivity analysis of a crack in an anisotropic material, where $\mathbf{M}(\mathbf{X})$ defines the mean fiber direction with the angle $\alpha = 45[^\circ]$ related to the x –axis in the material, u_{y0} defines the fixed bottom edge of the specimen with $u_x = 0$ and $u_y = 0$, and an applied uniaxial extension force at the top of the plate, which leads to a displacement u_y . All dimensions are given in [mm]. Adapted from the study of Gültekin et al. (2018) .

The results of this simulation were further compared with the results of the anisotropic fracture model for brittle solids under small strains proposed by Teichtmeister et al. (2017). In order to make a comprehensive comparison, the material for this simulation was assumed to behave brittle during rupture. This property was assured by the use of unit parameters for the shear modulus μ [kPa], the stress–like parameter k_1 [kPa] and the dimensionless parameter k_2 [–], the latter once are defined for the first fiber family with unit parameters. For the bulk modulus $\kappa = 3.0$ [kPa] was considered. The regularized critical energy release rate for fracture were defined for the isotropic material by $g_c^{\text{iso}}/l = 10^{-2}$ [kPa] and for the anisotropic material by $g_c^{\text{ani}}/l = 10^{-2}$ [kPa]. With the definition of the length–scale parameter $l = 0.1$ [mm] of the diffusive crack phase–field, the minimum mesh size parameter

$h[\text{mm}]$ has to be chosen to satisfy $l > 2h$.

With this in mind, the geometry was prepared with the software toolkit CUBIT[®] Release (2017) and furthermore a two-dimensional finite element mesh was applied on the geometry and was considered with 38800 quadrilateral elements, which were connected by 39295 nodes for the discretized domain.

To simulate the behavior of a brittle fracture in the material the artificial viscosity parameter η was additionally set to zero and the load was applied until the elastic range of the material reached its maximum ($d \approx 1$). After this point was reached in the loading curve, the unloading phase was initiated and the force $F[10^{-3}\text{N}]$ was decreased until the simulation crashed. This loading and unloading procedure was simulated for several values of the anisotropy parameter $-1 < \omega_M \leq 500$. This parameter directly affects the evolution of the crack path (Eq.(2.34)) depending on the second-order structure tensor (2.11), where the second fiber family is neglected for the simulation. This leads to a new form for the structure tensor, i.e.

$$\mathcal{L} = l^2[\mathbf{I} + \omega_M \mathbf{M} \otimes \mathbf{M}]. \quad (3.3)$$

Depending on Eq. (3.3), Eq. (2.10)₂ was reformulated to identify the crack surface density in the single-edge domain, which leads to the expression

$$\gamma(d, \nabla d; \mathcal{L}) = \frac{d^2}{2l} + \frac{l}{2} \nabla d \cdot \nabla d + \frac{l}{2} \omega_M (\nabla d \cdot \mathbf{M})(\mathbf{M} \cdot \nabla d), \quad (3.4)$$

where the third term on the right-hand side of this equation defines the anisotropic penalty term for the isotropic crack surface density with ω_M as the anisotropic penalty parameter. Based on Eq. (3.4) a sensitivity study for the anisotropy parameter ω_M was performed (see Fig. 3.8) to investigate the angle of the crack path θ for an anisotropic material. In the case $\omega_M \rightarrow \infty$, the crack was assumed to align along the fiber direction and enforces the term $(\nabla d \cdot \mathbf{M}) = 1$. Figure 3.8(a) also shows an important behavior of the crack path, for the anisotropy parameter of $\omega_M \approx -1$ a kink in the crack growth was observed. This may be caused by the limitation of ω_M in the negative range, to ensure the ellipticity condition and the possible minima of the energy of the crack path. For the anisotropy parameter $\omega_M \geq 10$ an apparent issue with the stability of the simulation was noticed. This effected the pattern of the crack growth and caused a termination of the simulation before the crack entirely permeated the continuum. Since the focus of this study was to define the crack growth with finite strains it was also assumed that this behavior determined in the study of Teichtmeister et al. (2017) with infinite strains. The major difference between this study and the study of Teichtmeister et al. (2017) is the prediction of the crack angle θ . Teichtmeister et al. (2017) used for the prediction of θ the proposed maximum energy release rate (MERR) concept from the study of Takei et al. (2013) used Wulff's plot to graphically construct crystal growth. For the graphical construction the inverse of the surface energy cost for fracturing in the material G_c as a polar plot and the energy release rate $G(\theta)$. The propagation direction defined by a linear plot, dependent on the loading and is tangent to the polar plot, were used (Takei et al., 2013). The intersection of both functions specify the angle of the crack propagation in an anisotropic material. Since this method is more

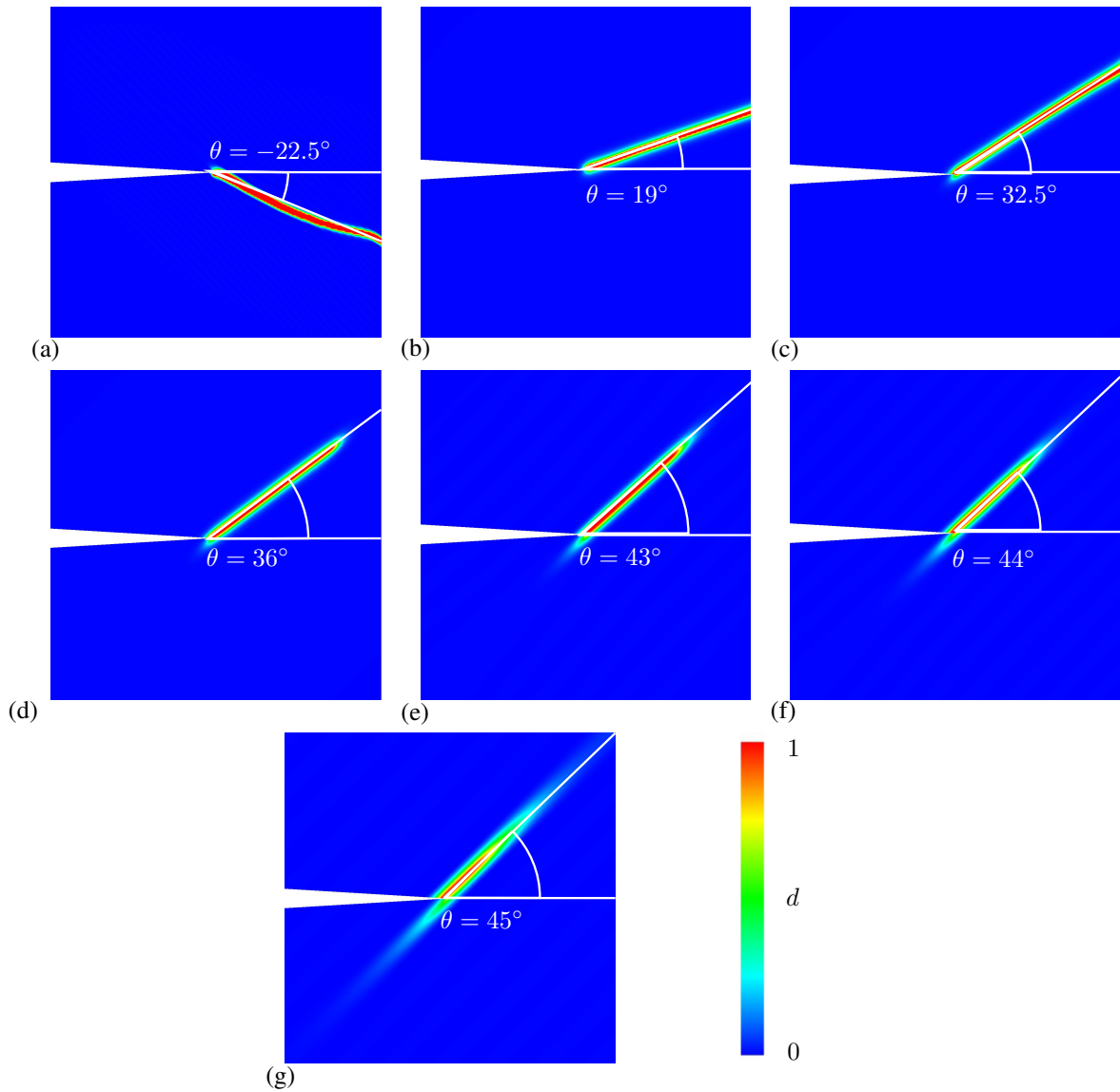


Figure 3.8.: Diffusive crack propagation defined by the crack angle θ in a brittle material with varying anisotropy parameter ω_M , e.g., (a) $\omega_M \approx -1$; (b) $\omega_M = 1$; (c) $\omega_M = 5$; (d) $\omega_M = 10$; (e) $\omega_M = 50$; (f) $\omega_M = 100$; (g) $\omega_M = 500$. Adapted from Gültekin et al. (2018).

representative for small strains the application for finite strains leads to high inaccuracies in the prediction of the crack path.

In addition to the investigation of the crack angle θ , the influence of the anisotropy parameter ω_M on the maximum loaded force with respect to the displacement was studied. Figure 3.9 exhibits a linear increasing of the force F with the corresponding increase of the displacement u_y until an initial rupture in the material occur, for a corresponding node, at the upper edge of the single–edge–notched domain. To ensure stability for each case of the simulation the time steps were decreased from 10^{-3} after the transition from the elastic range to values between 10^{-6} and 10^{-8} . Depending on the stability of the simulation larger time steps are more preferred to minimize the costs.

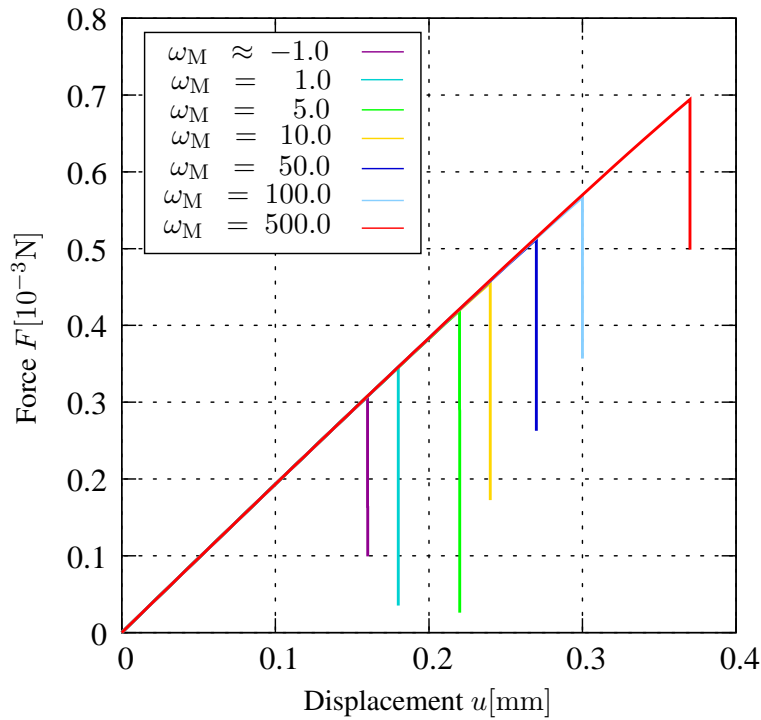


Figure 3.9.: Force-displacement curve of a node localized at the upper edge of the single–edge–notched geometry with respect to different values for the anisotropy parameter ω_M . Adapted from Gültekin et al. (2018).

In Fig. 3.9, it can be seen that an increase of the anisotropy penalty parameter ω_M corresponds to an increase of the crack angle θ and an increase of the displacement of the upper edge of the geometry. This behavior can be explained for the lower range of ω_M in which the force F is applied to the crack surface orthogonal. In these cases a lower displacement of the finite elements in this region was required to achieve the critical energy release rate for a crack growth. Greater values of ω_M lead to higher values for the geometric resistance of the material against crack growth due to larger values for the effective length–scale parameter, see Gültekin et al. (2016). To overcome this resistance higher forces are required to generate a fracture. For the analysis of the sensitivity of the crack angle θ related to

the anisotropy penalty parameter ω_M , the resulting crack angle θ from Fig. 3.8 was plotted with respect to ω_M , see Fig. 3.10. It may be ascertained, that above a certain value of ω_M a saturation behavior of the crack angle θ arises. Physically, this behavior can be explained with, that with a high anisotropy parameter the crack propagation will be perfectly aligned to the fiber direction \mathbf{M} . This behavior can be determined for values $\omega_M > 100$ in Fig. 3.10, and was also observed by Teichtmeister et al. (2017).

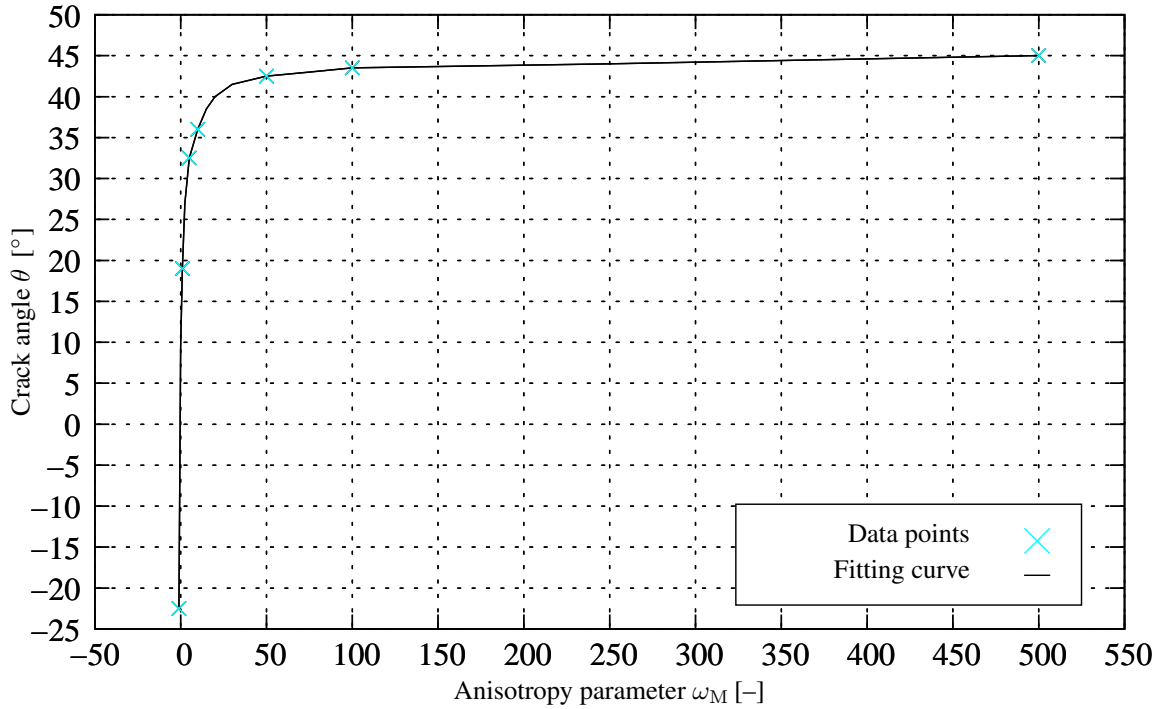


Figure 3.10.: Sensitivity of the crack angle θ versus the anisotropy parameter ω_M . Adapted from Gültekin et al. (2018).

In addition to the above investigated cases for ω_M , the case $\omega_M = -1$ was also evaluated and an unexpected crack path was observed. In addition, the crack path of $\omega_M \approx -1$ in Fig. 3.8(a) is the only crack propagation which indicates a kink. Since $\omega_M = -1$ defines the lower limit of ω_M , it is assumed that the ellipticity condition of the crack phase-field is no longer ensured. Furthermore it is assumed that the bending of the crack path occurs due to different directions but of equivalent values to minimize the energy in the domain.

In the analysis of the force F related to the displacement u_y the special case for a purely isotropic material with $\omega_M = 0$ was not included. This exception was made on the basis of the observation that a crack path not only relates to the anisotropy penalty parameter ω_M for the crack phase-field but is also dependent on the selected material model. For $\omega_M = 0$ a crack angle $\theta = 0$ was prior expected and not achieved in the posterior analysis, see Fig. 3.10. Since the crack driving source term \mathcal{H} in Eq. (2.27) is directly related to the effective free energy Ψ_0 of the material model, a value of ω_M leads to an isotropic crack resistance, but the crack driving force still possesses anisotropy. In Fig. 3.11, the influence

of the boundary of the domain is demonstrated. The closer the crack approaches the edge, the more parallel the crack starts to propagate with respect to the x -axis.

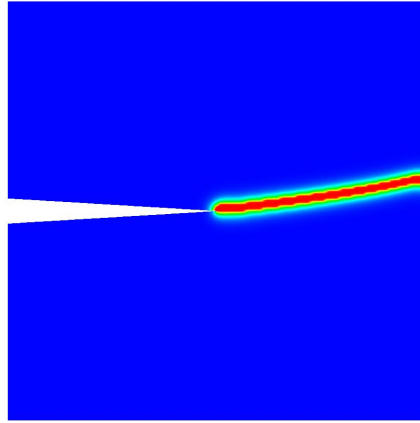


Figure 3.11.: Diffusive crack propagation defined by the crack angle θ in a brittle material with anisotropy parameter $\omega_M = 0$.

3.4. Application to aortic dissection

Based on the parameter identification in Sec. 3.1 and with respect to the sensitivity analysis of the anisotropic parameter ω_M in Sec. 3.3 the proposed model for fracture by Gültekin et al. (2018), summarized in Chap. 2, was applied on a three-dimensional cylindrical domain to investigate aortic dissection.

3.4.1. Geometry and material

To model an aortic dissection boundary-value problem, the biological domain has to be simplified to implement it later into FEAP[®] Release (2008). This simplification was done by the use of a multi-layered cylindrical shape domain, which contains of a combination of medial and adventitial layers. Figure 3.12 presents a schematic overview of the simplified biological domain, with the different sub-layers of the media, represented from the lumen outwards by the colors pink, blue, cyan and green, and the adventitial sub-layers defined by the colors yellow and orange. Note, that the third layer of the media (media 3) is defined as a degenerated sub-layer. This property is classified by the lower parameter values defined by the experimental study of Sommer et al. (2008). The dimensions of the idealized cylindrical tube were based on the study of Mao et al. (2008), which specified the dimensions of an ascending aorta for the application in the simulations. With this in mind a domain with the length of $h = 40[\text{mm}]$ and for the inner and outer radii, i.e. $R_i = 15$ and $R_o = 17.5[\text{mm}]$, which were measured during the end-diastolic phase of a cardiac cycle.

The thickness of each of the medial sub-layers is assumed by $t_{\text{med}} = 0.375[\text{mm}]$ and for the two remaining adventitial layers by $t_{\text{adv}} = 0.5[\text{mm}]$.

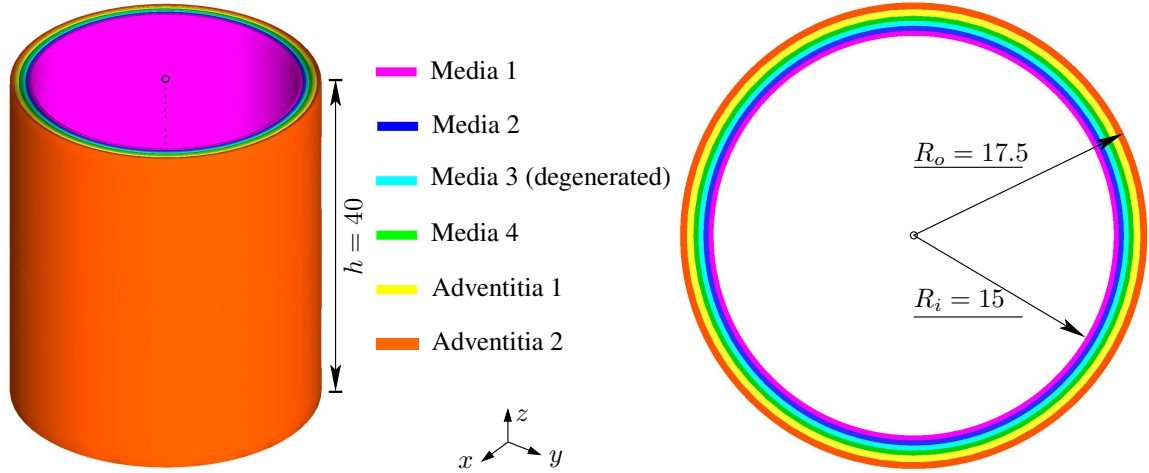


Figure 3.12.: Idealized geometry of an ascending aortic segment with multiple sub-layers of the media and the adventitia. From the lumen outwards the cylinder is composed of four layers of media defined by the colors pink, blue, cyan and green, and two layers of adventitia shown in yellow and orange. The green medial layer 4 is also specified as a degenerated layer, which is defined with lower stiffness. All dimensions are given in [mm]. Adapted from Gültekin et al. (2018).

Related to an aortic dissection problem, an initial damage is a priori implemented with a specific tear-size and tear-shape. This damage penetrated the wall of the cylinder until the sub-medial-layer media 4. This enabled a simulation as close as possible to the biological situation in the body. In the circumferential direction the tear-size was assumed to span with varying length $\pi R_i \beta / 180^\circ$, $\beta \in \{30^\circ, 60^\circ\}$, and a modifying size in the longitudinal direction, with $w_1 = 1$, $w_2 = 2$ and $w_3 = 4$ [mm], see Fig. 3.13. Since the study of Sommer et al. (2008) defined the mechanical properties of a degenerated medial sub-layer, defined as media 3 in this study, the parameters μ , k_1 and k_2 for a healthy medial sample are assumed to be 20 percent higher in relation to the material parameters of the diseased media 3, which leads to Table 3.3. Based on the parameter estimation in Section 3.1 for the degen-

Table 3.3.: Elastic and anisotropic mechanical and crack phase-field parameters related to the individual sub-layers for an extension-inflation-torsion test.

Layer	μ [kPa]	k_1 [kPa]	k_2 [-]	α [°]	g_c^{iso}/l [kPa]	g_c^{ani}/l [kPa]	ω_M [-]
Healthy media	100.21	121.9	5.00	44.70	100	300	10^3
Degraded media	83.50	101.65	4.17	44.70	6	18	10^3
Adventitia	200	400	4	44.7051	100	300	10^3

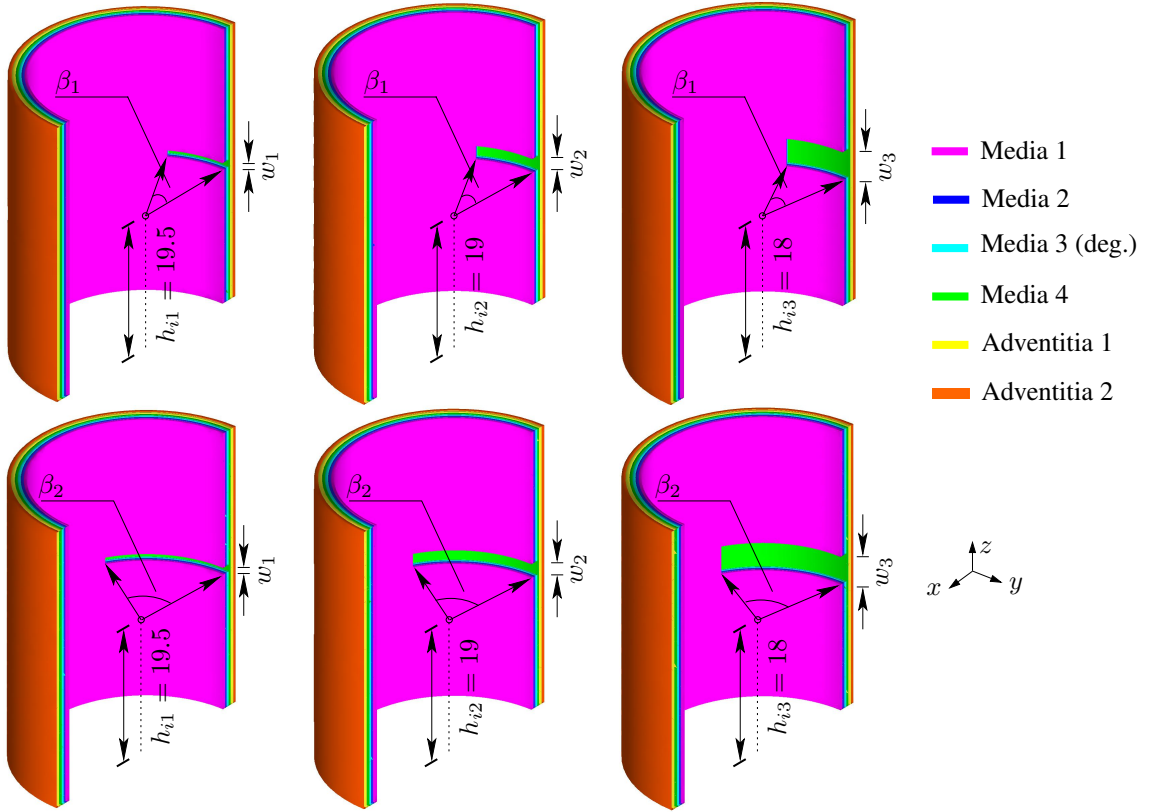


Figure 3.13.: Idealized geometry of Fig. 3.12 with varying angles and width of an incision. This initial defect is applied in the radial direction until it penetrates the degenerated Media 3. The angle β_i , $i \in \{1, 2\}$, defined in the circumferential direction, where $\beta_1 = 30$ and $\beta_2 = 60$ [°]. The width of the incision is represented by w_i , $i \in \{1, 2, 3\}$, with $w_1 = 1$, $w_2 = 2$ and $w_3 = 4$ [mm]. All dimensions are given in [mm]. Adapted from Gültekin et al. (2018).

erated media the mechanical properties for the healthy medial sub-layers media 1, media 2 and media 4 are defined. For the material parameters of the adventitia sub-layers we estimated respectively higher values, due to the high biological stiffness of these layers. The definition of the crack phase-field parameters by experiments is rather difficult, because of the effect of the sample size to rupture. Based on this it is more common in this research field to apply arbitrary values for the ratio g_c^i/l than classify parameters from experimental studies. From the previous performed sensitivity study of ω_M in Sec. 3.3, a value for the anisotropic parameter ω_M in the saturation range ($\omega_M = 10^3$ [-]) was presumed to enforce a crack propagation along the fiber direction.

3.4.2. Mesh and fiber direction

The related mesh to the defined geometries in Section 3.4.1 is composed of four–node tetrahedral elements, with different numbers of nodes and elements related to the specified geometry of the initial–tear, seen in Table 3.4. In addition, a constant length–scale parameter of $l = 0.1875[\text{mm}]$ was assumed, which leads to a conventional mesh geometry represented in Fig. 3.14. For the simplification of the biological domain, the fiber direction of the two different families \mathbf{M} and \mathbf{M}' are fitted as well to experimental data (Sommer et al., 2008), and are defined by the parameter $\alpha = 44.71[^\circ]$, for both families, represented by Fig. 3.15.

Table 3.4.: Total number of nodes and elements with respect to assumed geometry of the initial–tear geometry, defined by w and β represented in Fig. 3.13.

Geometry	# of nodes	# of elements
$\beta = 30^\circ, w = 1$	20 383	102 795
$\beta = 30^\circ, w = 2$	20 109	101 400
$\beta = 30^\circ, w = 4$	18 799	94 423
$\beta = 60^\circ, w = 1$	21 672	108 691
$\beta = 60^\circ, w = 2$	20 943	105 571
$\beta = 60^\circ, w = 4$	20 408	101 953

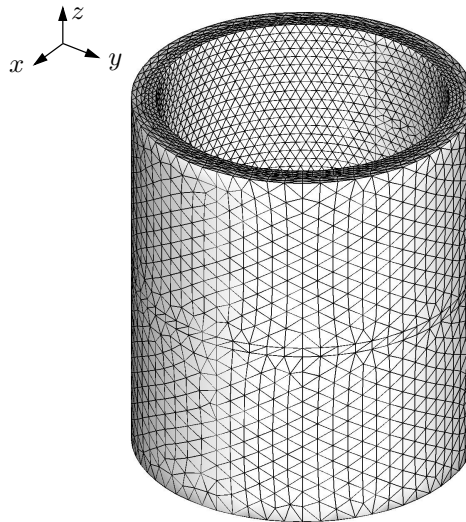


Figure 3.14.: Idealized cylindrical domain with a finite element mesh of tetrahedral elements. Adapted from Gültekin et al. (2018).

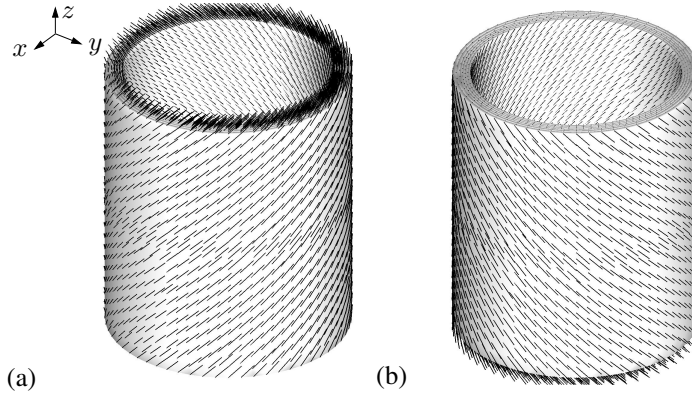


Figure 3.15.: Idealized cylindrical domain with representative mean fiber vectors: (a) first fiber family direction \mathbf{M} ; (b) second fiber family direction \mathbf{M}' . Adapted from Gültekin et al. (2018).

3.4.3. Boundary and loading conditions

The predefined cylindrical geometry undergoes a specified testing protocol. During the simulation the bottom plane of the domain is restricted against deformation in every direction by the boundary condition $u_x = u_y = u_z = 0$, see Fig. 3.16(a). The testing protocol describes two loading cycles, where the first one is defined in the physiological range of the blood pressure, while the second one describes a loading cycle in the supra-physiological range. More accurately, the pressure \hat{p} in the aorta inside the lumen, which affects the endothelium and generates a gradient over the cylindrical wall layers, acts in the first cycle, starts with 80[mmHg] and increases to a peak value of 120[mmHg]. The supra-physiological state cycle is defined by its peak value of 600[mmHg].

Figure 3.16(b) visualises the sequence with a saw-tooth pattern of one physiological state cycle followed by one supra-physiological state cycle. Since an aortic dissection is often associated with hypertension, it was assumed that rupture only occurs during the supra-physiological cycle, the peak value of this region is identified to appear during extreme sport exercises like weight-lifting, as mentioned by Kenney et al. (2015). After the pressure \hat{p} is reached the peak for the supra-physiological state decreases linearly to a physiological value $\hat{p} = 80$ [mmHg] at the end of the simulation.

Schulze-Bauer et al. (2003) observed in their study that the aortic tissue in the biological environment exhibits a pre-stretching, which leads to an axial deformation of 0 during a cardiac cycle. For the definition of the pre-stretched state of the artery the study by Horný et al. (2014) was used as the basis for the definition of the axial deformation $\hat{u}_z = 8$ [mm] in the biological environment, which further defines the stretch in the longitudinal direction, with $\lambda_z = 1.2$ related to the undeformed domain (Fig. 3.12). This situation was implemented during a linear increase of the axial displacement \hat{u}_z during the physiological part of the loading cycle until it reaches the biological prestretched value at the peak of the physiological loading state and remained constant during the sequence, see Fig. 3.16(c).

During a cardiac cycle, in general, the aorta performs a twisting defined by the angle $\hat{\phi}$ in the range of 8–12[°] (Carreras et al., 2012) in the case of a healthy left ventricle, this angle changing spreads further to the ascending part of the aorta, which was investigated in the present study, see Fig. 3.16(d). For the supra-physiological loading state a higher twisting angle was assumed with a maximum value of 30[°] and afterwards it decreases linearly, to the initial state of $\hat{\phi} = 0$ [°] at the end of the simulation.

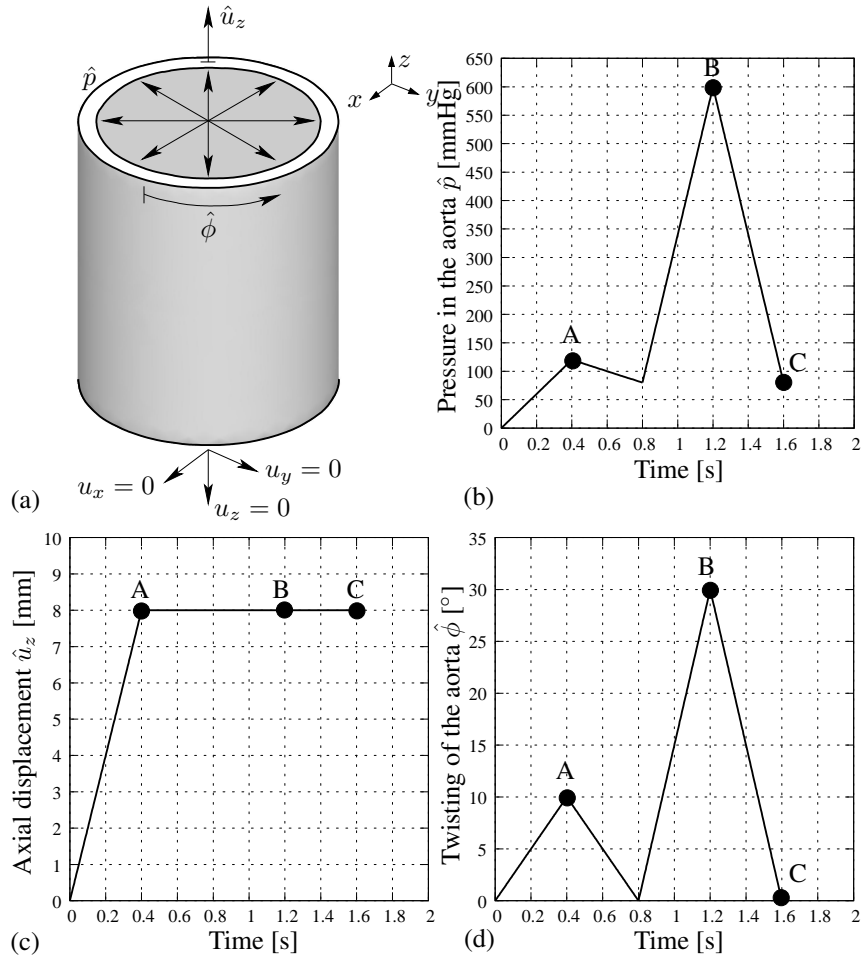


Figure 3.16.: (a) Idealized cylindrical domain with restricted bottom $z = 0$ mm, in the x -, y - and z -directions, with the option of torsion on the upper edge $z = 40$ mm; the loading conditions applied on the upper edge for the extension–inflation–torsion test defined by a physiological and a supra-physiological loading cycle, which are applied one after the other in a saw-tooth manner with respect to (b) pressure in the aorta \hat{p} ; (c) axial displacement \hat{u}_z (pre-stretching of the aorta in the first seconds and then remains constant); (d) twisting of the aorta defined by the angle $\hat{\phi}$. A, B and C defines the stages of the test at time $t \in \{0.4, 1.2, 1.6\}$, where A and B represents the peak of the physiological and supra-physiological state, and C marks the end of the simulation. Adapted from Gültekin et al. (2018).

3.4.4. Simulation and numerical results

With respect to the described loading procedure in Section 3.4.3 a simulation was executed with a starting time step–size of $\tau = 10^{-2}[\text{s}]$ which was decreased to $\tau = 10^{-4}[\text{s}]$, after stability issues have appeared to provide a crack initiation in the cylindrical domain. Figure 3.17 displays the crack phase–field evolution in the defined three–dimensional domain at the loading cycle peaks of the physiological state (A), the supra–physiological state (B) and at the end of the loading sequence (C).

Particularly, Fig. 3.17 visualizes the isosurface of the crack phase–field $d \geq 0.8$, which means it displays the damage zone of the domain close to the ruptured state ($d = 1$) between the degenerated medial sub–layer media 3 and a healthy medial sub–layer media 4, for varying tear–size and –shape. It is apparent, that none of the defined initial tear–shapes generates efficient high stress values during the physiological loading cycle to initiate a crack propagation around the initial tear. In addition, the top view of the domain (see Fig. 3.18) validates the intact state of the domain close to the border of the initial tear.

With an increase of the aortic pressure \hat{p} and $\hat{\phi}$, an initiation of the crack around the initial tear was observed due to a higher concentration of stress. With a large value of the anisotropic parameter $\omega_M = 1000$ a crack propagation along the first mean fiber direction was enforced. The sensitivity for the crack propagation with respect to the anisotropy was observed in Section 3.3. For case B Fig. 3.17 shows the cack phase–field with respect to $d \geq 0.8$. Furthermore, Fig. 3.18 displays a crack propagation along the circumferential direction, combined with the propagation along the fibers. A helical crack growth was observed in the cylindrical domain. After an increase of the loading condition to the instant C, a damaged zone was still noticed with values for the crack phase–field variable d above the isosurface 0.8. Due to this loss of integrity, the mechanical stiffness of the arterial sub–layers gets weaker in this region. With every supra–physiological cardiac cycle blood jets in this area, and therefore the healthy layers media 1, media 2 and the degenerated sub–layer media 3 are peeled off from the remaining layers. This separation of the layers leads to the creation of a false lumen beside the true lumen and can also block the true lumen when it reaches a significant size. Compared to the tear–size, defined by the value w , it was recognized that higher values for this variable were related to a higher stress concentration in the tissue. This appeared to be the case in in Fig. 3.17 (c) and (d) at instant B as larger damage zones than in Fig. 3.17 (a) and (b), with a smaller tear–size at the same time.

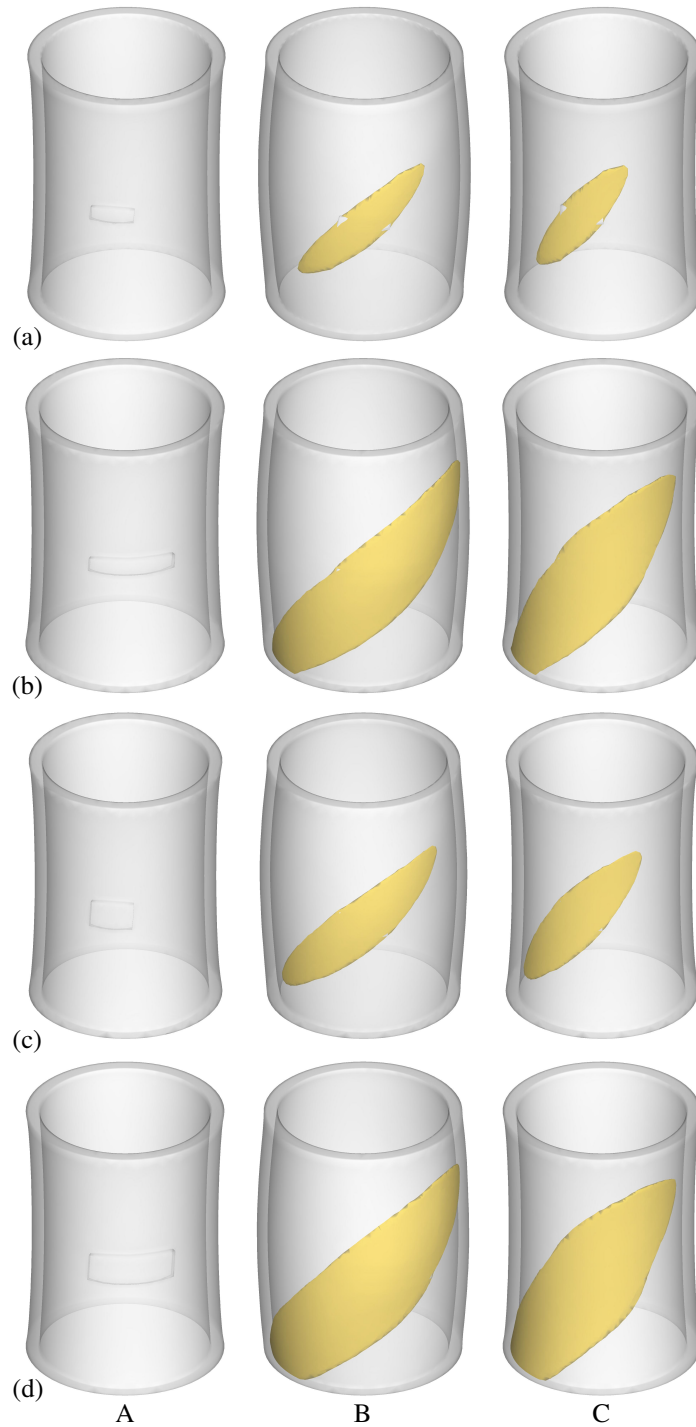


Figure 3.17.: Evolution of the crack phase-field between a diseased medial sub-layer media 3 and a healthy medial sub-layer media 4 at the peak values of the physiological/supra-physiological states, related to the loading cycle in Fig. 3.16 with respect to varying tear-size and tear-shape (a) $w = 2[\text{mm}]$, $\beta = 30[^\circ]$; (b) $w = 2[\text{mm}]$, $\beta = 60[^\circ]$; (c) $w = 4[\text{mm}]$, $\beta = 30[^\circ]$; (d) $w = 4[\text{mm}]$, $\beta = 60[^\circ]$. With an isosurface value $d \geq 0.8$, to visualize a damage zone close to the ruptured state. Adapted from Gültekin et al. (2018).

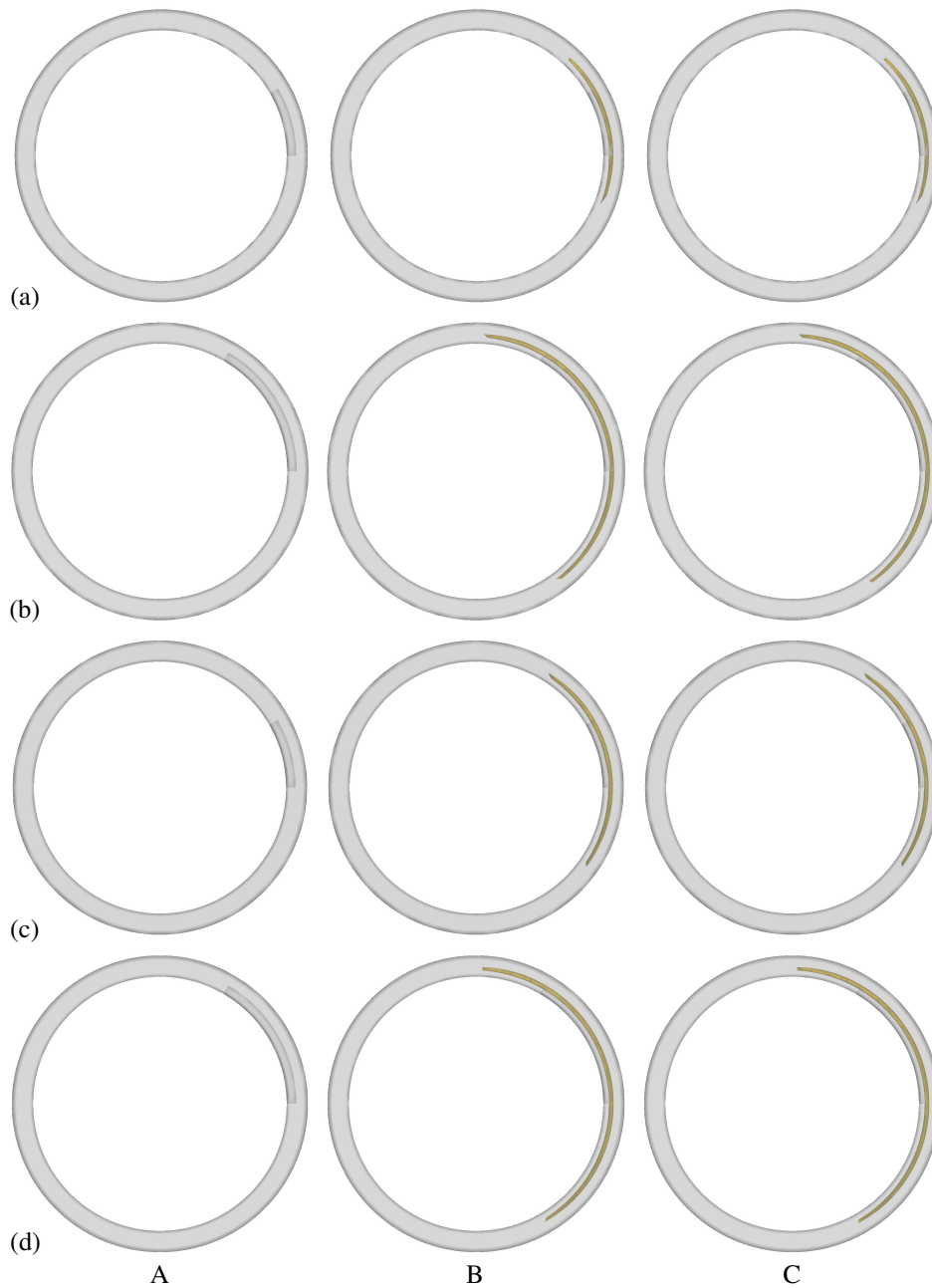


Figure 3.18.: Evolution of the crack phase-field between a diseased medial sub-layer media 3 and a healthy medial sub-layer media 4 displayed in the cross-section at the peak values of the physiological/supra-physiological states, related to the loading cycle in Fig. 3.16 with respect to varying tear-size and tear-shape (a) $w = 2[\text{mm}]$, $\beta = 30[^\circ]$; (b) $w = 2[\text{mm}]$, $\beta = 60[^\circ]$; (c) $w = 4[\text{mm}]$, $\beta = 30[^\circ]$; (d) $w = 4[\text{mm}]$, $\beta = 60[^\circ]$. With an isosurface value $d \geq 0.8$, to visualize a damage zone close to the ruptured state. Adapted from Gültekin et al. (2018).

4. Conclusion

With an increasing amount of cardiovascular diseases, especially diseases which affect the aorta, it is important to develop new methods to define the mechanical stresses in arteries. Based on the parameter identification of the mechanical properties by the use of high-resolution medical imaging methods, it is possible to apply the obtained material parameters to simulations which represent the in vivo situation in the body. The method of simulation is becoming more and more necessary in these times to reduce the amount of experiments to a minimum, and also to make predictions about the course of a disease in a patient. With the focus on the prediction part the aim is to produce patient-specific models in the near future, for example, for the case of an aortic dissection. The present study showed that an aortic dissection initiates around a defined initial tear and propagates in a helically pattern between two sub-layers of the aorta. The location where the dissection starts is further dependent on the radial depth of the initial tear in the aorta. In this study the *a priori* defined initial tear in the mesh interferes with the lumen and a predefined mechanical degenerated medial sub-layer. With the discussed model, it was possible to recreate the same helical crack propagation in the longitudinal direction in the simulations as it was observed in different experimental investigations. Compared to other anisotropic models, it is important to note that the introduced second-order tensor \mathcal{L} , which is dependent on the anisotropy parameters ω_M and ω'_M , has no influence on the crack driving source term for the crack phase-field d . As a next step, the investigation of the anisotropy parameters $\omega_M = 0$ and $\omega'_M = 0$ in regard to a different constitutive model would be interesting in order to see if the crack propagation still prefers a certain direction in relation to another.

Bibliography

- T. L. Anderson. *Fracture mechanics: Fundamentals and Applications*. Taylor & Francis, 2005.
- C. Van Baardwijk, M. R. Roach. Factors in the propagation of aortic dissections in canine thoracic aortas. *J. Biomech.*, 20:67–73, 1987.
- F. Carreras, J. Garcia–Barnes, D. Gil, S. Pujadas, C. H. Li, R. Suarez–Arias, R. Leta, X. Alomar, M. Ballester, and G. Pons–Llado. Left ventricular torsion and longitudinal shortening: two fundamental components of myocardial mechanics assessed by tagged cine-MRI in normal subjects. *Int. J. Cardiovasc. Imaging.*, 28:273–284, 2012.
- M. W. Carson, M. R. Roach. The strength of the aortic media and its role in the propagation of aortic dissection. *J. Biomech.*, 23:579–588, 1990.
- K. J. Cherry Jr. and M. D. Dake. *Comprehensive Vascular and Endovascular Surgery (Second Edition)*. J. W. Hallett, J. L. Mills, J. J. Earnshaw, J. A. Reekers, and T. W. Rooke. *Aortic Dissection* Mosby, Philadelphia, 2009.
- A. Delfino, N. Stergiopoulos, J. E. Moore, and J. J. Meister. Residual strain effects on the stress field in a thick wall finite element model of the human carotid bifurcation. *J. Biomech.*, 30:777–786, 1997.
- CUBIT Release 2017. Sandia National Laboratories, USA, 2017.
- H. Demiray. A layered cylindrical shell model for an aorta. *Int. J. Eng. Sci.*, 29:47–54, 1991.
- D. W. Dunning, J. K. Kahn, E. T. Hawkins, and W. W. O’Neill. Iatrogenic coronary artery dissections extending into an involving the aortic root. Catheter. *Catheter Cardiovasc. Interv.*, 51:387–393, 2000.
- FEAP – A finite element analysis, Version 8.2. University of California at Berkely, Berkely, California, USA, 2008.
- A. Ferrara and A. Pandolfi. A numerical study of arterial media dissection processes. *Int. J. Fracture*, 166:21–33, 2010.
- Y. C. Fung, K. Fronek, and P. Patitucci. Pseudoelasticity of arteries and the choice of its mathematical expression. *Am. J. Physiol.*, 237:H620–H631, 1979.

- C. T. Gasser and G. A. Holzapfel. Modeling the propagation of arterial dissection. *Eur. J. Mech. A–Solid*, 25:617–633, 2006.
- C. T. Gasser, R. W. Ogden and G. A. Holzapfel. Hyperelastic modelling of arterial layers with distributed collagen fibre orientations. *J. R. Soc. Interface.*, 3:15–35, 2006.
- A. A. Griffith. The phenomena of rupture and flow in solids. *Philos. Trans. A Math. Phys. Eng. Sci.*, 221:163–198, 1920.
- O. Gültekin, H. Dal, G. A. Holzapfel. A phase-field approach to model fracture of arterial walls: Theory and finite element analysis. *Comput. Methods Appl. Mech. Eng.*, 312: 542–566, 2016.
- O. Gültekin, H. Dal, G. A. Holzapfel. Crack phase-field modeling of anisotropic rupture in fibrous soft tissues. *XIV International Conference on Computational Plasticity. Fundamentals and Applications*, COMPLAS XIV, E. Oñate, D.R.J. Owen, D. Peric and M. Chiumenti (Eds), 2017.
- O. Gültekin, H. Dal, G. A. Holzapfel. Numerical aspects of anisotropic failure in soft biological tissues favor energy-based criteria: A rate dependent anisotropic crack phase-field model. *Comput. Method. Appl. M.*, 331:23–52, 2018.
- O. Gültekin, S. P. Hager, H. Dal, G. A. Holzapfel. Computational modeling of progressive damage and rupture in fibrous biological tissues: Application to aortic dissection. *submitted*
- H. W. Haslach Jr., and R. Armstrong. *Deformable Bodies and their Material Behavior*. John Wiley & Sons, NY, 2004.
- H. W. Haslach Jr., A. Siddiqui, A. Weerasooriya, R. Nguyen, J. Roshgadol, N. Monforte, and E. McMahon Fracture mechanics of shear crack propagation and dissection in the healthy bovine descending aortic media. *Acta Biomater.*, 68:53–66, 2018.
- L. F. Hiratzka, G. L. Bakris. ACCF/AHA/AATS/ACR/ASA/SCA/SCAI/SIR/STS/SVM Guidelines for the Diagnosis and Management of Patients with Thoracic Aortic Disease. *Catheter Cardiovasc. Interv.*, 121:266–369, 2010.
- G. A. Holzapfel and H. W. Weizsäcker. Biomechanical behavior of the arterial wall and its numerical characterization. *Comput. Biol. Med.*, 28:377–392, 1998.
- G. A. Holzapfel. *Nonlinear Solid Mechanics. A Continuum Approach for Engineering*. John Wiley & Sons, Chichester, 2000.
- G. A. Holzapfel, T. C. Gasser, and R. W. Ogden. A new constitutive framework for arterial wall mechanics and a comparative study of material models. *J. Elasticity*, 61:1–48, 2000.

- G. A. Holzapfel, G. Sommer, C. T. Gasser, and P. Regitnig. Determination of layer-specific mechanical properties of human coronary arteries with nonatherosclerotic intimal thickening and related constitutive modeling. *Am. J. Physiol. Heart Circ. Physiol.*, 289: H2048–H2058, 2005.
- L. Horný, M. Netušil, and T. Voňavková. Axial prestretch and circumferential distensibility in biomechanics of abdominal aorta. *Biomech. Model Mechanobiol.*, 13:783–799, 2014.
- IRAD International Registry of Acute Aortic Dissections. <http://www.iradonline.org/irad.html>, 1996.
- G. R. Irwin. Fracture Dynamics. *Fracturing of Metals, American Society of Metals*, 147–166, 1948.
- G. R. Irwin. Onset of fast crack propagation in high strength steel and aluminium alloys. *Sagamore Research Conference Proceedings*, 2:289–305, 1956.
- G. R. Irwin. Analysis of stresses and strains near the end of a crack traversing a plate. *J. Appl. Mech.*, 27:361–364, 1957.
- D. L. Kasper, A. S. Fauci, D. L. Longo, S. L. Hauser, J. L. Jameson, and J. Loscalzo. *Harrison's Principle of Internal Medicine*. 19th ed. McGraw-Hill Professional, NY, 2015.
- W. L. Kenney, J. H. Wilmore, and D. L. Costillo. *Physiology of Sport and Exercise*. 6th Human kinetics, Champaign, IL, 2015.
- W. W. Von Maltzahn, D. Besdo, and W. Wiemer. Elastic properties of arteries: A nonlinear two-layer cylindrical model. *J. Biomech.*, 14:389–397, 1981.
- S. S. Mao, N. Ahmadi, B. Shah, D. Beckmann, A. Chen, L. Ngo, F. R. Flores, Y. I. Gao, and M. J. Budoff. Normal thoracic aorta diameter on cardiac computed tomography in healthy asymptomatic adult; Impact of age and gender. *Acad. Radiol.*, 15:827–834, 2008.
- M. Marino, and G. Vairo. Influence of inter-molecular interactions on the elasto-damage mechanics of collagen fibrils: A bottom-up approach towards macroscopic tissue modeling. *J. Mech. Phys. Solids*, 73:38–54, 2014.
- MATLAB Release 2016b. The MathWorks Inc., Natick, MA, USA, 2016.
- C. Miehe, F. Welschinger, and M. Hofacker. Thermodynamically consistent phase-field models of fracture: Variational principles and multi-field FE implementations. *Int. J. Numer. Meth. Eng.*, 83:1273–1311, 2010.

- C. Miehe, M. Hofacker, and F. Welschinger. A phase field model for rate-independent crack propagation: Robust algorithmic implementation based on operator splits. *Comput. Method. Appl. Mech. Eng.*, 199:2765–2778, 2010.
- B. Mikich. Dissection of the aorta: a new approach. *Heart*, 89:6–8, 2003.
- F. F. Mussa, J. D. Horton, R. Moridzadeh, J. Nicholson, S. Trimarchi, and K. A. Eagle. Acute aortic dissection and intramural hematoma: A systematic review. *JAMA*, 316:754–763, 2016.
- C. Noble, O. van der Sluis, R. M.J. Voncken, O. Burke, S. E. Franklin, R. Lewis, and Z. A. Taylor. Simulation of arterial dissection by a penetrating external body using cohesive zone modelling. *J. Mech. Behav. Biomed. Mater.*, 71:95–105, 2017.
- S. Numata, K. Itatani, K. Kanda, K. Doi, S. Yamazaki, K. Morimoto, K. Manabe, K. Ike-moto, and H. Yaku. Blood flow analysis of the aortic arch using computational fluid dynamics. *Eur. J. Cardiothorac. Surg.*, 49:1578–1585, 2016.
- J. Pepper. Differential aspects of the disease and treatment of Thoracic Acute Aortic Dissection (TAAD) - The European experience. *Ann. Cardiothorac. Surg.*, 5:360–367, 2016.
- A. Rachev. Theoretical study of the effect of stress-dependent remodeling on arterial geometry under hypertensive conditions. *J. Biomech.*, 30:819–827, 1997.
- A. Rachev and K. Hayashi. Theoretical study of the effects of vascular smooth muscle contraction on strain and stress distributions in arteries. *Ann. Biomed. Eng.*, 27:459–468, 1999.
- J. R. Rice. A path independent integral and the approximate analysis of strain concentration by notches and cracks. *J. Appl. Mech.*, 35:379–386, 1968.
- M. H. Ross and W. Pawlina. *Histology: A Text and Atlas, with Correlated Cell and Molecular Biology*. Lippincott Williams & Wilkins, Baltimore, 2011.
- Tecplot 360 2017 R3. Tecplot Inc., Bellevue, WA, USA, 2017.
- S. Teichtmeister, D. Kienle, F. Aldakheel, and M. A. Keip. Phase-field modeling of fracture in anisotropic brittle solids. *Int. J. Nonlin. Mech.*, 97:1–21, 2017.
- A. Tsamis, J. T. Krawiec, D. A. Vorp. Elastin and collagen fibre microstructure of the human aorta in ageing and disease: A Review. *J. R. Soc. Interface*, 10:20121004, 2013.
- A. J. Schriebl, G. Zeindlinger, D. M. Pierce, P. Regitnig and G. A. Holzapfel. Determination of the layer-specific distributed collagen fibre orientations in human thoracic and abdominal aortas and common iliac arteries. *J. R. Soc. Interface*, 9 :1275–1286, 2012.

- C. A. J. Schulze–Bauer, C. Mörth, and G. A. Holzapfel. Passive biaxial mechanical response of aged human iliac arteries. *J. Biomech. Eng.*, 125 :395–406, 2003.
- C. F Shih, and J. W. Hutchinson. Fully plastic solutions and large-scale yielding estimates for plane stress crack problems. *J. Eng. Mater–T. Asme.*, 98:289–295, 1976.
- G. Sommer, T. C. Gasser, P. Regitnig, M. Auer, and G. A. Holzapfel. Dissection properties of the human aortic media: An experimental study. *J. Biomech. Eng.*, 130:021007-1–021007-021012, 2008.
- G. Sommer, S. Sherifova, P. J. Oberwalder, O. E. Dapunt, P. A. Ursomanno, A. DeAnda, B. E. Griffith, and G. A. Holzapfel. Mechanical strength of aneurysmatic and dissected human thoracic aortas at different shear loading modes. *J. Biomech.*, 49:2374–2382, 2016.
- L. G. Svensson and E. S. Crawford. Aortic dissection and aortic aneurysm surgery: Clinical observations, experimental investigations, and statistical analyses, Part II. *Curr. Probl. Surg.*, 29:923–1011, 1992.
- A. Takei, B. Roman, J. Bico, E. Hamm, and F. Melo. Forbidden directions for the fracture of thin anisotropic sheets: An analogy with the Wulff plot. *Phys. Rev. Lett.*, 110:144301–1–144301–5, 2013.
- S. Teichtmeister, D. Kienle, F. Aldakheel, and M. A. Keip. Phase-field modeling of fracture in anisotropic brittle solids. *Int. J. Nonlin. Mech.*, 97:1–21, 2017.
- R. N. Vaishnav, J. T. Young, and D. J. Patel. Distribution of stresses and of strain-energy density through the wall thickness in a canine aortic segment. *Circ. Res.*, 32:577–583, 1973.

Appendices

A. Modeling of soft biological tissue in the Lagrangian configuration

To model arterial wall mechanics the constitutive framework from Holzapfel et al. (2000) was used. In addition, it was assumed that the material shows an incompressible behavior, the material keeps the volume constant through $J = 1$.

A.1. Incompressible material

A.1.1. Helmholtz free energy $\Psi(J, I_1, I_4, I_6)$

This section specifies the stored energy Ψ_i with $i \in \{\text{vol}, \text{ani}, \text{iso}\}$ in the material, i.e.

$$\Psi(J, I_1, I_4, I_6) = \Psi_{\text{vol}}(J) + \Psi_{\text{iso}}(I_1) + \Psi_{\text{ani}}(I_4, I_6), \quad (\text{A.1})$$

where $\Psi_{\text{vol}}(J)$ describes the volumetric elastic response of the material, $\Psi_{\text{iso}}(I_1)$ defines the isochoric or volume-preserving elastic term of the material and $\Psi_{\text{ani}}(I_4, I_6)$ specifies the finite elastic response of fiber-reinforced composites. The volumetric term and the isochoric term are in the model of Gültekin et al. (2018) combined to

$$\Psi_{\text{iso}}(J, I_1) = \Psi_{\text{vol}}(J) + \Psi_{\text{iso}}(I_1), \quad (\text{A.2})$$

where $\Psi_{\text{iso}}(J, I_1)$ specifies the isotropic part from the neo-Hookean hyperelastic model, which models the ground matrix of the material with

$$\Psi_{\text{vol}}(J) = \kappa(J - \ln(J) - 1) \quad \text{and} \quad \Psi_{\text{iso}}(I_1) = \frac{\mu}{2}(I_1 - 2\ln(J) - 3), \quad (\text{A.3})$$

where κ describes the bulk modulus and μ classifies the shear modulus of the material, both parameters should be adjusted to reach a level for Poisson's ratio ν close to 0.5 to ensure incompressibility of the material, i.e.

$$0 < \nu = \frac{3\kappa - 2\mu}{2(3\kappa + \mu)} < 0.5. \quad (\text{A.4})$$

For the anisotropic response that features the hyperelasticity of two fiber families distributed in the ground matrix the term

$$\Psi_{\text{ani}}(I_4, I_6) = \frac{k_1}{2k_2} \sum_{i=4,6} \{ \exp[k_2(I_i - 1)^2] - 1 \} \quad (\text{A.5})$$

is introduced, where $k_1 > 1$ describes a stress-like material parameter and $k_2 > 0$ specifies a dimensionless parameter.

A.1.2. Stress tensor \mathbf{S}

To obtain a solution for nonlinear problems in finite elasticity for computational problems, the computed elasticity tensor \mathbb{C} will be implemented in the finite element code. For the calculation, the Helmholtz free energy $\Psi(J, I_1, I_4, I_6)$ is derived with respect to the right Cauchy–Green tensor \mathbf{C} , i.e.

$$\mathbf{S} = \mathbf{S}_{\text{vol}} + \mathbf{S}_{\text{iso}} + \mathbf{S}_{\text{ani}}, \quad (\text{A.6})$$

where \mathbf{S}_{vol} , \mathbf{S}_{iso} and \mathbf{S}_{ani} defines the volumetric, isochoric and the anisotropic second Piola–Kirchhoff stress tensor, respectively. With the calculated $\mathbf{S}(J, I_4, I_6)$ it is possible to calculate the Cauchy stress tensor $\boldsymbol{\sigma}$, with the relation $\boldsymbol{\sigma} = J^{-1} \mathbf{F} \mathbf{S} \mathbf{F}$. The volumetric stress tensor \mathbf{S}_{vol} can be derived by

$$\mathbf{S}_{\text{vol}} = 2\partial_{\mathbf{C}}\Psi_{\text{vol}} = 2\partial_J\Psi_{\text{vol}}\partial_{\mathbf{C}}, \quad (\text{A.7})$$

with $\partial_{\mathbf{C}}J = \frac{1}{2}J\mathbf{C}^{-1}$ and $\Psi'_{\text{vol}} = \frac{\kappa}{J}(J-1)$, which leads to the final form

$$\mathbf{S}_{\text{vol}} = \kappa(J-1)\mathbf{C}^{-1} \quad (\text{A.8})$$

for the volumetric term. The volume–preserving term \mathbf{S}_{iso} of the total stress tensor $\mathbf{S}(J, I_4, I_6)$ will be calculated with

$$\mathbf{S}_{\text{iso}} = 2\partial_{\mathbf{C}}\Psi_{\text{iso}} = 2(\partial_{\mathbf{C}}\Psi_{\text{iso}}(J) + \partial_{\mathbf{C}}\Psi_{\text{iso}}(I_1)), \quad (\text{A.9})$$

where

$$\partial_{\mathbf{C}}\Psi_{\text{iso}}(J) = \Psi'_{\text{iso}}(J) \underbrace{\partial_{\mathbf{C}}J}_{\frac{1}{2}J\mathbf{C}^{-1}} = -\frac{\mu}{2}\mathbf{C}^{-1} \quad \text{and} \quad \partial_{\mathbf{C}}\Psi_{\text{iso}}(I_1) = \Psi'_{\text{iso}}(I_1) \underbrace{\partial_{\mathbf{C}}I_1}_{\mathbf{I}} = \frac{\mu}{2}\mathbf{I} \quad (\text{A.10})$$

which leads to the final form for the isochoric stress tensor \mathbf{S}_{iso} , i.e.

$$\mathbf{S}_{\text{iso}} = \mu(\mathbf{I} - \mathbf{C}^{-1}), \quad (\text{A.11})$$

where \mathbf{I} defines the identity matrix. For simplicity the calculation anisotropic term is shown only for the fiber direction \mathbf{M} , i.e.

$$\mathbf{S}_{\text{ani}} = 2\partial_{\mathbf{C}}\Psi_{\text{ani}}(I_4) = 2\Psi'_{\text{ani}}(I_4)\partial_{\mathbf{C}}I_4, \quad (\text{A.12})$$

with

$$\partial_{\mathbf{C}}I_4 = \mathbf{M} \otimes \mathbf{M} = \mathbf{A}_4 \quad \text{and} \quad \Psi'_{\text{ani}}(I_4) = k_1(I_4 - 1)\exp[k_2(I_4 - 1)^2], \quad (\text{A.13})$$

where $\mathbf{A}_{\mathbf{M}}$, $\mathbf{M} = 4, 6$ is the second–order structure tensor of the fiber–reinforced material. With that it is possible to generate a readable form of the anisotropic stress tensor \mathbf{S}_{ani} , i.e.

$$\mathbf{S}_{\text{ani}} = 2k_1 \sum_{i=4,6} (I_i - 1) \exp[k_2(I_i - 1)^2] \mathbf{A}_i. \quad (\text{A.14})$$

A.1.3. Elasticity tensor \mathbb{C}

To achieve the final form of the elasticity tensor \mathbb{C} , which defines the stiffness of the domain in the finite element method, the stress tensor \mathbf{S} is derived with respect to the right Cauchy–Green tensor \mathbf{C} and can be written in the decoupled form

$$\mathbb{C} = \mathbb{C}_{\text{vol}} + \mathbb{C}_{\text{iso}} + \mathbb{C}_{\text{ani}}(I_4, I_6), \quad (\text{A.15})$$

where \mathbb{C}_{vol} , \mathbb{C}_{iso} and \mathbb{C}_{ani} are the volumetric, isochoric and anisotropic contributions to the elasticity tensor \mathbb{C} . The pure volumetric term can be written in the form

$$\mathbb{C}_{\text{vol}} = 4\partial_{\mathbf{C}\mathbf{C}}^2 \hat{\Psi}_{\text{vol}} = 4\partial_{\mathbf{C}}(\partial_J \Psi_{\text{vol}} \partial_{\mathbf{C}} J) = 4[\underbrace{\partial_{JJ}^2 \Psi_{\text{vol}}}_{\Psi''_{\text{vol}}} \partial_{\mathbf{C}} J \otimes \partial_{\mathbf{C}} J + \underbrace{\partial_J \Psi_{\text{vol}}}_{\Psi'_{\text{vol}}} \partial_{\mathbf{C}\mathbf{C}}^2 J], \quad (\text{A.16})$$

where Ψ''_{vol} and Ψ'_{vol} specifies the second and first derivative of the Helmholtz free energy, with

$$\Psi''_{\text{vol}} = \kappa \frac{1}{J^2} \partial_{\mathbf{C}\mathbf{C}}^2 J = \partial_{\mathbf{C}} \left(\frac{1}{2} J \mathbf{C}^{-1} \right) = \frac{1}{2} (\partial_{\mathbf{C}} J \otimes \mathbf{C}^{-1} + J \underbrace{\partial_{\mathbf{C}\mathbf{C}} \mathbf{C}^{-1}}_{-\mathbb{I}_{\mathbf{C}^{-1}}}), \quad (\text{A.17})$$

where $\mathbb{I}_{\mathbf{C}^{-1}}$ describes a fourth order identity matrix. The final form of the volumetric term of the elasticity tensor is then defined as

$$\mathbb{C}_{\text{vol}} = \kappa [\mathbf{C}^{-1} \otimes \mathbf{C}^{-1} + (J - 1) \mathbf{C}^{-1} \otimes \mathbf{C}^{-1} - 2(J - 1) \mathbb{I}_{\mathbf{C}^{-1}}]. \quad (\text{A.18})$$

For the purely isotropic contribution of the elasticity tensor, i.e.

$$\mathbb{C}_{\text{iso}} = 2\partial_{\mathbf{C}} \mathbf{S}_{\text{iso}}(\mathbf{C}^{-1}) = 2\partial_{\mathbf{C}^{-1}} \mathbf{S}_{\text{iso}}(\mathbf{C}^{-1}) \partial_{\mathbf{C}} \mathbf{C}^{-1}, \quad (\text{A.19})$$

with

$$\partial_{\mathbf{C}} \mathbf{C}^{-1} = \mathbb{I}_{\mathbf{C}^{-1}} \quad \text{and} \quad \partial_{\mathbf{C}^{-1}} \mathbf{S}_{\text{iso}}(\mathbf{C}^{-1}) = -\mu \mathbf{I}, \quad (\text{A.20})$$

the result is then

$$\mathbb{C}_{\text{iso}} = 2\mu \mathbb{I}_{\mathbf{C}^{-1}}. \quad (\text{A.21})$$

Also for simplification, only the calculation for the anisotropic contribution of the elasticity tensor is show. From the fiber direction \mathbf{M} we obtain

$$\mathbb{C}_{\text{ani}}(I_4) = 4\partial_{\mathbf{C}}^2 \Psi_{\text{ani}}(I_4) = 4\partial_{I_4 I_4}^2 \Psi_{\text{ani}}(I_4) \partial_{\mathbf{C}} I_4 \otimes \partial_{\mathbf{C}} I_4, \quad (\text{A.22})$$

with

$$\Psi''_{\text{ani}}(I_4) = k_1 \exp[k_2(I_4 - 1)^2] [1 + 2k_2(I_4 - 1)^2] \quad \text{and} \quad \partial_{\mathbf{C}} I_4 \otimes \partial_{\mathbf{C}} I_4 = \mathbf{A}_4 \otimes \mathbf{A}_4, \quad (\text{A.23})$$

which leads to the final form of

$$\mathbb{C}_{\text{ani}}(I_4, I_6) = 4k_1 \sum_{i=4,6} \exp[k_2(I_i - 1)^2] [1 + 2k_2(I_i - 1)^2] \mathbf{A}_i \otimes \mathbf{A}_i, \quad (\text{A.24})$$

which can further be implemented in the stiffness matrix of the element.

B. Implementation in a finite element code

This chapter briefly describes the implementation of the proposed model by Gültekin et al. (2016), for more details see Gültekin et al. (2016),(2018) and Miehe et al. (2010). This section, briefly describes the general procedure to achieve the weak form of a strong formulation of the governing equation by applying the Galerkin method to derive from the strong formulation of the Eq.(2.25) and (2.34) the weak formulation to apply on the discretized domain of the system. Through an operator–splitting algorithm the non–convex multi–field problem is decoupled in two convex problem sets with the internal variables $\varphi(\mathbf{X}, t)$ and $d(\mathbf{X}, t)$. These fields are then solved by a Newton–Raphson solver for the nodal degrees of freedom.

B.1. Temporal discretization

For the discretization process the field variables are only considered at discrete times in the simulation interval $t_n \in [0, T]$, with $n \in [0, \infty]$. As step size $\tau = t_{n+1} - t_n$ is considered, where t_n defines the previous time step and t_{n+1} represents the current time step. For the definition of the current field, all field variables from the previous step have to be known.

B.2. Spatial discretization

As soon a temporal discretization is applied on the scheme an algorithm can be used to define the spatial discretised field variables. Through an operator–splitting algorithm the non–convex multi–field problem (ALGO_{CM}) is decoupled in two convex problem sets with the internal variables $\varphi(\mathbf{X}, t)$ (ALGO_{M}) and $d(\mathbf{X}, t)$ (ALGO_{C}), i.e.

$$\text{ALGO}_{\text{CM}} = \text{ALGO}_{\text{C}} \circ \text{ALGO}_{\text{M}}, \quad (\text{B.1})$$

which leads to a robust and stable algorithm for the simulation, for further details see Gültekin et al. (2017) and Miehe et al. (2010).

B.2.1. Spatial discretization for the mechanical problem

For the computation of the mechanical problem a Newton–type iteration solver is applied to the Eulerian equation of the minimization problem of the elasticity by neglecting the term of the crack phase–field variable. The solution of the discretization was based on the algorithmic form of the variational problem for the nodal position vector \mathbf{d}_φ in the compact notation proposed by Miehe et al. (2010), i.e.

$$\mathbf{d}_\varphi \Leftarrow \mathbf{d}_\varphi - \left(\int_{\mathcal{B}^h} \mathbf{B}_\varphi^T [\partial_{\mathbf{c}_\varphi^h}^2 \pi_\varphi^\tau(\mathbf{c}_\varphi^h)] \mathbf{B}_\varphi dV \right)^{-1} \int_{\mathcal{B}^h} \mathbf{B}_\varphi^T [\partial_{\mathbf{c}_\varphi^h} \pi_\varphi^\tau(\mathbf{c}_\varphi^h)] dV, \quad (\text{B.2})$$

where \mathbf{B}_φ^T describes the global interpolation matrix composed by the specified shape functions and its derivatives, with \mathbf{c}_φ^h defined as the state vector of the deformation map and the gradient of it, and π_φ^τ represents the algorithmic potential energy function for the mechanical problem defined over the interpolated domain \mathcal{B}^h .

B.2.2. Spatial discretization for the phase–field problem

In order to discretize the domain for the phase–field problem, the same procedure as in Section B.2.1 described is used. For the calculation of the nodal phase–field vector \mathbf{d}_d a further equation can be used to solve an arbitrary boundary–value problem, i.e.

$$\mathbf{d}_d = \left(\int_{\mathcal{B}^h} \mathbf{B}_d^T [\partial_{\mathbf{c}_d^h}^2 \pi_d^\tau(\mathbf{c}_d^h)] \mathbf{B}_d dV \right)^{-1} \int_{\mathcal{B}^h} \mathbf{B}_d^T [\partial_{\mathbf{c}_d^h} \pi_d^\tau(\mathbf{c}_d^h)] dV, \quad (\text{B.3})$$

where \mathbf{B}_d^T , \mathbf{c}_d^h , π_d^τ and \mathbf{c}_d^h describe the same variables as previously mentioned for the mechanical problem, now they represent the variables for the phase–field problem.